PAPER

Check for updates

Fabrication and characterization of rare earth-free nanophosphor based devices for solid-state lighting applications†

M. Rakshita,[a] Aachal A. Sharma,[a] Payal P. Pradhan,[a] K. A. K. Durga Prasad,[a] M. Srinivas[b] and D. Haranath (ID) *[a]

This study presents a novel, rare-earth-free $Zn_3V_2O_8$ nanophosphor (ZnVO NP) with exceptional luminescent properties, making it ideal for phosphor-converted white light-emitting diodes (pc-WLEDs). When coupled with a 385 nm LED chip, ZnVO NP delivers white light with a correlated color temperature of approximately 4920 K, a high quantum yield of 74%, and an excellent color rendering index (CRI) of R_a = 91. Notably, the R_9 value of 90.5 surpasses that of commercially available $Y_3Al_5O_{12}:Ce^{3+}$ (R_9 = 14.3), highlighting superior red color rendering. The white light, excited at 385 nm, has CIE coordinates of (0.330, 0.301). Temperature-dependent photoluminescence spectra indicate high thermal stability, with emission peaking in the yellow region at CIE coordinates (0.43, 0.52) under 290 nm, 361 nm, and 385 nm excitation. This broadband yellow-emitting ZnVO NP offers a promising rare-earth-free alternative for pc-WLEDs, providing excellent color quality and stability under diverse operating conditions, demonstrating its practical potential in advanced lighting applications.

1. Introduction

Commercial solid-state lighting (SSL) has widely adapted white light-emitting diodes (WLEDs) due to their enhanced luminous efficiency (LE) and long lifespan. Traditionally, white light production in WLEDs involves coating a yellow-emitting phosphor ($Y_3Al_5O_{12}:Ce^{3+}$,YAG) onto a blue (InGaN) LED chip. However, differences in the aging properties of the blue (410–460 nm) LED chip and the yellow (570–590 nm) phosphor can lead to instability in white light production by the combination of these two complementary colors (yellow and blue).[1–4] Furthermore, this type of white LED emits negligible red light, leading to a low color rendering index (CRI < 70) and a high correlated color temperature (CCT > 6000 K).[5–7] To address these issues, a mixture of red, green, and blue (RGB) phosphors combined with a near-ultraviolet (NUV) LED chip (370–420 nm) can be employed to produce stable white light. In this setup, the visible components of white light are generated entirely by the phosphors, which exhibit minimal variation in color output under different forward-bias currents. NUV LED chips, particularly at 380 nm, are attractive due to their excellent energy

conversion efficiency.[8] All three phosphors (RGB) must efficiently absorb in the NUV region for optimal device performance. However, the commonly used rare-earth metal ion, Ce^{3+}, is susceptible to oxidation, has limited availability, is costly, and is a non-renewable resource. Therefore, exploring rare-earth-free, yellow-emitting materials with excellent LE and stable thermal and chemical properties is essential.[9] WLEDs that utilize a NUV LED chip, combined with UV LED and yellow-red emitting phosphors, are increasingly favored for their higher CRI, adjustable CCT, and ideal white CIE color coordinates. Consequently, there is a growing demand in the WLED industry for the design and development of tunable yellow-red emitting phosphors that can be efficiently activated by NUV light.

In recent years, a wide range of inorganic materials, including tungstates, silicates, phosphates, borates, sulfides, molybdenites, and vanadates, have been explored for the development of high-performance luminescent materials.[9–23] Among these, vanadates particularly those derived from alkali or alkaline earth materials have garnered significant attention due to their excellent chromatic properties and potential applications in electrochemistry, display technology, photocatalysis, triboelectric nanogenerators, and SSL devices.[24–27] Vanadate-based, self-activated phosphors have emerged as promising candidates for WLED under near-ultraviolet (NUV) excitation.[28,29] The photoluminescent quantum yield (PLQY) of vanadates is highly dependent on the spacing between V^{5+}

[a] *Department of Physics, National Institute of Technology, Warangal 506 004, Telangana, India. E-mail: haranath@nitw.ac.in; Tel: +91 995 810 1115*

[b] *Department of Physics, Osmania University, Hyderabad-500007, Telangana, India*

† Electronic supplementary information (ESI) available. See DOI: https://doi.org/10.1039/d5ma00117j

luminescent centers.[30,31] However, crystal defects such as oxygen vacancies inevitably occur during high-temperature oxide synthesis and play a crucial role in determining the optoelectrical properties of these materials.[32,33] Studies have shown that oxygen vacancies influence the symmetry of octahedral structures, alter electron interactions, and contribute to structural disorder, resulting in changes to the optical, electrical, and magnetic properties of transition metal oxides (d-block elements).[34] These vacancies act as donors, affecting the oxidation state of cations and creating local chemical pressure within the structure.

One significant advantage of self-activated vanadate phosphors over rare-earth-based phosphors is their cost-effectiveness, which helps conserve global rare-earth resources. These vanadate compounds have gained considerable attention due to their ability to self-activate and produce a broad emission spectrum in the visible region, primarily driven by the intense metal-to-oxygen charge transfer (CT) transition from V^{5+} to O^{2-} within the VO_4 tetrahedron. Their strong absorption bands in the NUV range make them highly suitable for SSL applications. By carefully selecting the luminescent center and composition, it is possible to tailor the luminescence properties of vanadates. The VO_4^{3-} group, comprising four oxygen ions arranged in a tetrahedral configuration around a central vanadium ion, serves as the highly efficient light-emitting core.[35–37]

Nanophosphors (NPs) have gained significant attention due to their distinctive properties compared to bulk materials, including a large surface-to-volume ratio, drastically different physicochemical characteristics, and high porosity.[38] Metal vanadates ($M_xV_yO_z$, M = Co, Zn, Ni, Cu, Fe) represent a notable class of nanomaterials, attracting widespread research interest for their potential applications in WLEDs. The combination of the vanadate tetrahedral (T_d) symmetry with various metal elements such as Ag, Cu, Fe, and Pb offers a wide array of optical properties, improved thermochemical stability, and an economical, simple synthesis process that eliminates the need for rare-earth elements. Oxygen vacancies in vanadium oxides contribute to a mixed valency state of V^{4+} and V^{5+}, which adversely impacts PL.[39] This phenomenon highlights the importance of understanding how oxygen vacancies in the $[VO_4]$ tetrahedron influence the self-activation of phosphors. Extensive research has been conducted on synthesizing metal vanadates through various methods, including wet chemical approaches, hydrothermal techniques, coprecipitation, sol–gel, and solid-state reactions.[26,40,41] Among these, zinc vanadate nanomaterials have garnered significant interest due to zinc's environmental friendliness, abundance, low cost, and vanadium's multiple valence states, which enable the formation of complex architectures. Zinc vanadate ($Zn_3V_2O_8$) has shown promise in several fields, including photocatalysis, lithium-ion batteries, supercapacitors, and luminescent materials for WLEDs, largely due to its unique crystal structure (porous framework) as shown in ESI,† Table S1.[26,40]

Nakajima *et al.* have reported the PL and color properties of $M_3V_2O_8$ (M = Mg, Zn) and AVO_3 (A = K, Rb, Cs), synthesized *via* the solid-state method (SSM).[42] Similarly, Ni *et al.* described the

hydrothermal synthesis of $Zn_3V_2O_8$ microparticles using $Zn_3(OH)_2V_2O_7 \cdot nH_2O$ nanosheets as the starting material and investigated their optical properties.[43] Hydrothermal synthesis of vanadium-based materials in the presence of long-chain alkylamines typically results in 1D and 2D structures such as rods, wires, fibers, sheets, or ribbons, but this process often requires extended reaction times (over 24 hours). For large-scale production, a simpler, cost-effective approach is needed.

In this study, $Zn_3V_2O_8$ (ZnVO) NPs were synthesized using the sol–gel method (SGM), urea auto-combustion (UAC) method, coprecipitation method (CPM), and hydrothermal method (HTM). Among these, the CPM is one of the simplest and most economical techniques, where metal ions are transformed into the desired materials through a chemical reaction between metal nitrates and bases. This method offers advantages such as better homogeneity, a high surface-to-volume ratio, and higher purity. The broadband emission properties of $Zn_3(VO_4)_2$ synthesized by CPM were extensively studied in terms of structural, morphological, elemental, and optical characteristics and compared with those produced using SGM, UAC, and HTM.

2. Experimental section

2.1 Sol–gel method (SGM)

ZnVO NP was synthesized using the SGM with NH_4VO_3, $Zn(NO_3)_2 \cdot 6H_2O$, and citric acid as starting materials. A solution with a Zn : V molar ratio of 3 : 2 was prepared by dissolving 3 mol% of $Zn(NO_3)_2 \cdot 6H_2O$ and 2 mol% of NH_4VO_3 in 40 ml of deionized (DI) water. Citric acid, serving as the chelating agent, was added at a concentration of 0.05 mol%. The final solution was heated at 80 °C on a hot plate while being stirred continuously until all the water evaporated, forming a gel. This gel was then dried at 140 °C for 24 hours to yield $Zn_3V_2O_7(OH)_2 \cdot 2H_2O$ powder. The resulting powder was ground and subsequently calcined in a preheated furnace at 600 °C for 30 minutes to remove any remaining organic and inorganic compounds, forming the ZnVO NP, which was then subjected to further characterization.

2.2 Urea auto combustion method (UAC)

The UAC method involves rapidly heating a water-based solution containing stoichiometric proportions of ammonium nitrate, metal nitrates, and urea, which acts as a combustion fuel. ZnVO NP was synthesized using this method with $Zn(NO_3)_2 \cdot 6H_2O$, NH_4VO_3, and urea as starting precursors. These precursors were dissolved in DI water in their stoichiometric ratios and stirred at 80 °C until a clear, yellowish homogeneous mixture was obtained. The solution, placed in a quartz beaker, was then transferred to a preheated muffle furnace set at 600 °C for less than 30 minutes. During this process, the solution boiled, frothed, and ignited, resulting in the formation of the final product, which was subsequently ground and prepared for further characterization.

2.3 Co-Precipitation method (CPM)

ZnVO NP was synthesized using the CPM. A zinc nitrate solution (solution 1) was prepared by dissolving 0.03 mol of $Zn(NO_3)_2 \cdot 6H_2O$ in 30 ml of DI water. Simultaneously, an ammonium metavanadate solution (solution 2) with a $Zn:V$ molar ratio of $3:2$ was prepared by dissolving 0.02 mol of NH_4VO_3 in 20 ml of hot DI water (80 °C). The water facilitates hydrolysis, leading to the formation of metal hydroxides or intermediate compounds. After solution 2 cooled naturally to room temperature (RT), it was added dropwise to Solution 1 with continuous stirring. To adjust the pH to 10, 1 M NaOH was added gradually, and the mixture was stirred for 6 hours until a homogeneous yellow precipitate of $Zn_3V_2O_7(OH)_2 \cdot 2H_2O$ formed. Upon the addition of the precipitating agent, a chemical reaction took place, resulting in the formation of insoluble nanoparticles. The precipitate was collected by centrifugation at 6000 rpm and thoroughly washed several times with DI water and ethanol to remove unreacted components. It was then dried at 80 °C for 24 hours. Finally, ZnVO NPs were obtained by sintering the dried powder ($Zn_3V_2O_7(OH)_2 \cdot 2H_2O$) in an air atmosphere at 600 °C for less than 30 minutes to remove hydroxide moieties and crystallization water.

2.4 Hydrothermal method (HTM)

ZnVO NP was synthesized using the HTM with $Zn(NO_3)_2 \cdot 6H_2O$ and NH_4VO_3 as precursors. First, 0.03 mol of $Zn(NO_3)_2 \cdot 6H_2O$ and 0.02 mol of NH_4VO_3 were dissolved in 100 ml of DI water and stirred continuously to form a homogeneous solution. To adjust the pH to approximately 10, 1 M NaOH was added dropwise while the mixture was stirred on a magnetic hot plate at 80 °C for 3 hours. The resulting solution was then transferred to a 250 ml Teflon-lined autoclave and maintained at 180 °C for 12 hours. After natural cooling to RT, the final product was collected by centrifugation at 6000 rpm for 30 minutes, followed by multiple washings with water and ethanol. The collected sample was then dried at 80 °C and annealed at 600 °C for 30 minutes in a muffle furnace. For comparison, a ZnVO sample was also prepared using the SSM. ZnO and V_2O_5 were thoroughly mixed in a mortar and pestle and annealed at 800 °C for 1 hour.

It is understood that the synthesis method plays a crucial role in determining various properties of $Zn_3V_2O_8$ phosphors by influencing factors such as crystal structure, particle size, and surface defects. Among the various synthesis approaches discussed above, the co-precipitation method (CPM) has a profound impact on the photoluminescence (PL) properties of self-activated $Zn_3V_2O_8$, yielding the highest luminescence quantum yield (QY). This is primarily attributed to the controlled nucleation and rapid precipitation of Zn^{2+} and V^{5+} precursors, leading to ultrafine, homogeneous nanocrystals with minimal defects. The enhanced PL emission arises from the improved structural uniformity, reduced non-radiative recombination sites, and optimized charge transfer within the $[VO_4]^{3-}$ luminescent centers. In contrast, the solid-state reaction method, despite ensuring excellent phase purity and crystallinity, often results in larger particle sizes and a lower surface area, leading to weaker luminescence due to limited exciton confinement and increased defect-induced quenching. The sol–gel method, while effective in producing fine particles with controlled stoichiometry, can introduce residual organic species or trapped solvent molecules, which act as quenching centers, reducing luminescence efficiency. Compared to hydrothermal and urea auto-combustion methods, which also produce nanostructured phosphors, co-precipitation provides superior control over particle growth and surface passivation, significantly enhancing quantum efficiency. The ability to tailor the defect density, crystallite size, and luminescent center distribution through this method makes it a promising route for optimizing the self-activated emission of $Zn_3V_2O_8$ for high-performance phosphor-converted white light-emitting diodes.

2.5 Device fabrication of prototype LED

A WLED prototype was fabricated by combining ZnVO nanoparticles (NPs) with epoxy resin and a 385 nm LED chip. The resin and ZnVO NPs were mixed in a $3:7$ ratio and applied as a 200 μm thick layer onto a thin glass slide. The mixture was dried at 70–90 °C for 24 hours. The devices were then encapsulated with ZnVO NPs and mounted directly on the headers. The electroluminescence (EL) of the packaged LED device, embedded with ZnVO NPs, was measured using an integrating sphere after final assembly.

2.6 Instrumentation tools

The powder X-ray diffraction (PXRD) patterns of the samples were acquired in the 2θ range from 10° to 80° using Ni-filtered Cu Kα ($\lambda = 1.54$ Å) as a source of X-ray at a scan rate of 0.01 s^{-1} with Rigaku. The Fourier transform infrared spectrum (FTIR) of the samples was measured from 4000 to 400 cm^{-1} range using PerkinElmer (100S FTIR spectrophotometer) in KBr pellets with 4 cm^{-1} resolutions for 20 scans. The morphology of the samples was carried out by scanning electron microscopy (SEM) using ZEISS. In the elemental study, the atomic and weight proportion of the component ions were measured by energy dispersive X-ray spectroscopy (EDAX) attached with SEM. The solid-state absorption spectroscopy was analyzed using UV/visible-diffuse reflectance spectroscopy (UV/vis-DRS) by Analytic Jena with a wavelength range of 200–1000 nm equipped with an integrating sphere using $BaSO_4$ as standard. High-resolution X-ray photoelectron spectroscopy has been used to detect the ionic state of surface ions in hematite that uses a monochromatic Al Kα radiation source with an energy of ~1500 eV in the Thermo Scientific K alpha system. The C 1s peak at ~285 eV was used as a reference for sample charging correction of other elements. The photoluminescence excitation (PLE) and emission (PL) of the synthesized samples were recorded using HITACHI: fluorescence spectrophotometer F-4700. The Horiba Scientific Spectrophotometer: Fluorolog-3 is used to perform life decay and the TDPL of the samples. The EL of capped glass slides coated with ZnVO NPs was measured by using Spectra Wiz Integrated Sphere.

3. Results and discussion

3.1 Structural, morphological, and optical characterization

3.1.1 PXRD analysis. Fig. 1(a) PXRD patterns of ZnVO nanoparticles synthesized by SGM, UAC, CPM, and HTM methods compared to the standard pattern (JCPDS 34-0378). The diffraction peaks observed at 2θ values of $15.365°$, $18.741°$, $21.41°$, $26.45°$, $27.081°$, $29.455°$, $31.005°$, $34.911°$, $35.981°$, $36.465°$, $43.116°$, $43.302°$, $57.705°$, $58.442°$, $60.564°$, $62.974°$, and $64.608°$ correspond to the (020), (120), (200), (220), (211), (131), (040), (122), (320), (311), (042), (151), (162), (360), (004), (442), and (080) planes of the ZnVO phase. The shift of diffraction peaks to higher angles (right shift) indicates compression and a decrease in the average lattice parameter as shown in Fig. 1(b). All peaks are well-matched to the pure $Zn_3V_2O_8$ orthorhombic structure with space group $Cmca$ (space group number 64), and cell constants $a = 8.2990$ Å, $b = 11.5284$ Å, and $c = 6.1116$ Å, with $Z = 4$. No additional peaks were observed, confirming the high purity and excellent crystallinity of the ZnVO samples. Kurzawa *et al.* reported the presence of α and β phases of $Zn_3V_2O_8$, which form at lower and higher temperatures, respectively, with a transition temperature of 795 °C. According to Rakshita *et al.*, a stoichiometric mixture of ZnO

and V_2O_5 heated at 800 °C for 1 hour yields a pure phase of $Zn_3V_2O_8$.[25] The average crystalline size (D) and dislocation density (δ) of the synthesized samples were detected using the following eqn (1) and (2).[44,45]

$$D = \frac{K\lambda}{\beta \cos\theta} \text{ (nm)} \tag{1}$$

$$\delta = \frac{1}{D^2} \left(\frac{\text{lines}}{\text{m}^2} \right) \tag{2}$$

where β is the full-width half maxima (FWHM) intensity, K is the shape factor (0.9), θ is the Braggs angle, δ is the dislocation density, and λ is the wavelength of the Cu source employed in PXRD which normally assumes a value of about 1.54. The sample synthesized using CPM shows the lowest D value 22.73 nm, increasing by UAC > HTM and increase in the SGM synthesized sample. Likewise, strain broadening is calculated by, $\beta = 4\varepsilon\tan\theta$, where '$\varepsilon$' is the root mean square value of the micro-strain, d is the interplanar spacing, a, b, and c are the lattice constants and h, k, and l are the miller indices. As a result, the line broadening is a function of crystallite size and strain, as represented by the W–H equation using eqn (4),[46,47]
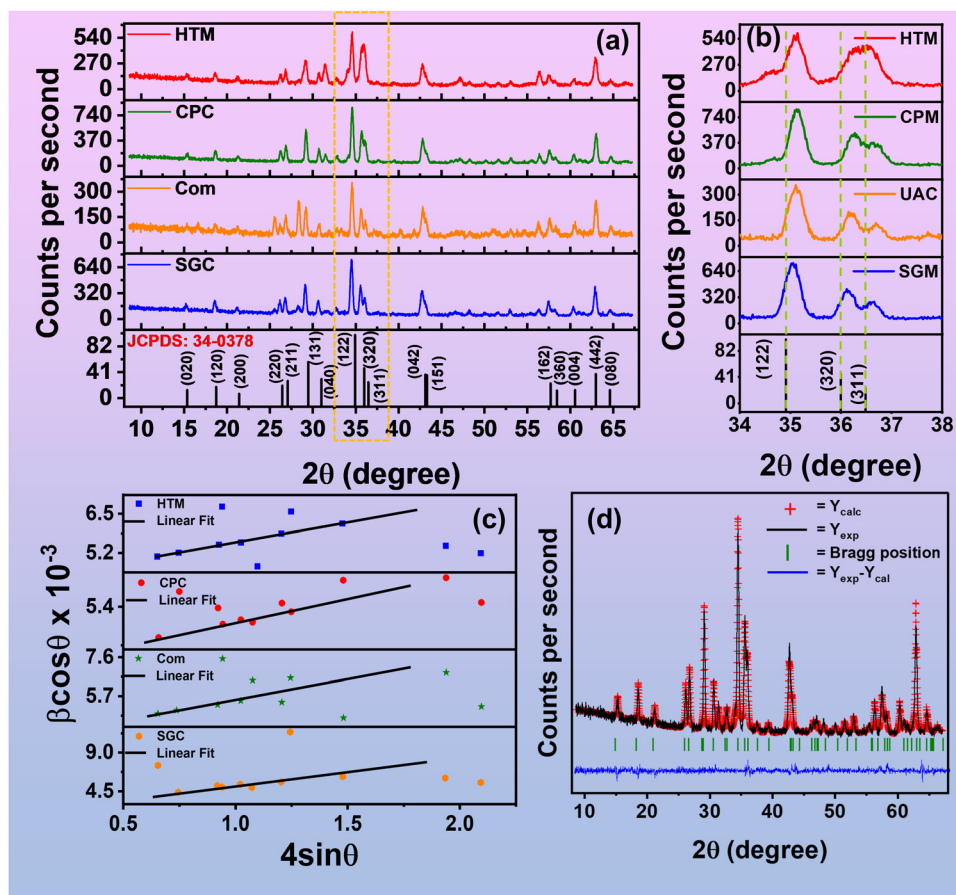

Fig. 1 PXRD patterns of ZnVO nanoparticles synthesized using different methods: (a) SGM, UAC, CPM, and HTM, (b) theta shift towards higher angles, (c) Williamson–Hall (W–H) plot, and (d) Rietveld refinement of the PXRD pattern for ZnVO nanoparticles synthesized *via* CPM.

and the lattice parameters of the pure ZnVO were calculated using eqn (5),[25] respectively as shown

$$\beta = \left(\frac{0.9\lambda}{D\cos\theta}\right) + 4\varepsilon\tan\theta \quad (3)$$

$$\beta\cos\theta = \left(\frac{0.9\lambda}{D}\right) + 4\varepsilon\sin\theta \quad (4)$$

$$\frac{1}{d^2} = \frac{h^2}{a^2} + \frac{k}{b^2} + \frac{l^2}{c^2} \quad (5)$$

The microstrain can be determined by plotting the value of $\beta\cos\theta$ as a function of $4\sin\theta$ shown in Fig. 1(c), and the crystalline size from the intersection with the vertical axis. For SGM, UAC, CPM, and HTM synthesized samples, the strain of ZnVO NPs is 2.27×10^{-3}, 1.56×10^{-3}, 0.99×10^{-3}, 1.3×10^{-3}, and the crystalline size is 22.52 nm, 22.66 nm, 22. 02 nm, and 22.68 nm respectively. Table S2 (ESI†) shows that the estimated values are well-matched with the standard values without much variation. The micro-strain in the CPM synthesized sample is lower than in HTM, UAC, and SGM synthesized samples. The less strain in the CPM method synthesized samples shows the synthesized ZnVO sample has high crystallinity and better ionic bonding. To additional validate the purity of the phase and lattice characteristics of the synthesized material, the crystal structure of the ZnVO CPM NP was derived using a Rietveld refinement fullprof software.[48] Fig. 1(d) depicts both the observed and calculated XRD profiles, all peaks have been indexed and the refinement is satisfactory. The most straightforward discrepancy index, the weighted profile R-factor (R_{wp}), follows directly from the square root of the quantity minimized, scaled by the weighted intensities (eqn (6)):

$$R_{wp}^2 = \frac{\sum_i w_i(y_{C,i} - y_{O,i})^2}{\sum_i w_i(y_{O,i})^2} \quad (6)$$

This "best possible R_{wp}" quantity is a very useful concept and is called the expected R factor (R_{exp}) (eqn (7)). Using N as a label for the number of data points

$$R_{exp}^2 = \frac{N}{\sum_i w_i(y_{O,i})^2} \quad (7)$$

That χ^2 (eqn (8)) can be determined from the weighted profile and expected R factors

$$\chi^2 = \left(\frac{R_{wp}}{R_{exp}}\right)^2 \quad (8)$$

The single-crystal literature often uses the term goodness of fit (G) which is defined by "$G^2 = \chi^2$". The ultimate refinement, as observed, converges to $R_{wp} = 2.05\%$, $R_p = 5.24\%$, $R_{exp} = 1.97\%$, and $\chi^2 = 1.08\%$.

3.1.2 FTIR analysis. The surface characteristics of synthesized ZnVO NPs were analyzed using FTIR spectroscopy to identify any residual organic compounds. Fig. 2 shows the
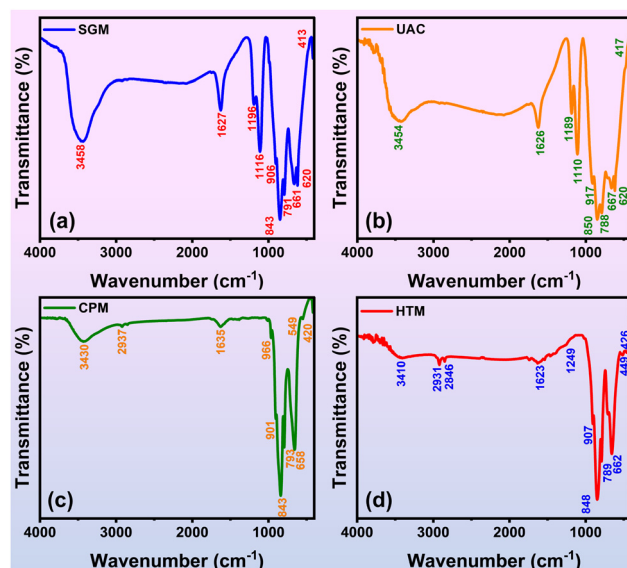

Fig. 2 FTIR spectra of ZnVO nanophosphors synthesized by different methods: (a) SGM, (b) UAC, (c) CPM, and (d) HTM.

FTIR spectra for ZnVO NPs synthesized by different methods (SGM, UAC, CPM, and HTM) after calcination. Here, we focus on the FTIR spectrum of the sample synthesized using the CPM method (Fig. 2(c)), with details of the other samples provided in Table 1. The absorption band centered at 3430 cm^{-1} corresponds to the bending and stretching vibrations of hydrogen-bonded O–H groups from adsorbed water. The peak at 793 cm^{-1} is associated with the T_d VO$_4$ vibration modes involving corner atoms in the network. Peaks at 658, 843, and 901 cm^{-1} are attributed to V–O–V bonds. A weaker peak at 549 cm^{-1} corresponds to the V–O–Zn bond, while the Zn–O bond vibration is observed at 420 cm^{-1}, related to the octahedral ZnO$_6$ structure.[49] Faint peaks around 2937 cm^{-1} and 1249 cm^{-1} are due to the symmetric and asymmetric stretching vibrations of aliphatic groups (–CH$_2$–)$_n$ respectively. A peak at approximately 1623 cm^{-1} indicates the presence of

Table 1 FTIR wavenumber ranges and corresponding functional groups present in ZnVO samples synthesized by SGM, UAC, CPM, and HTM methods after annealing

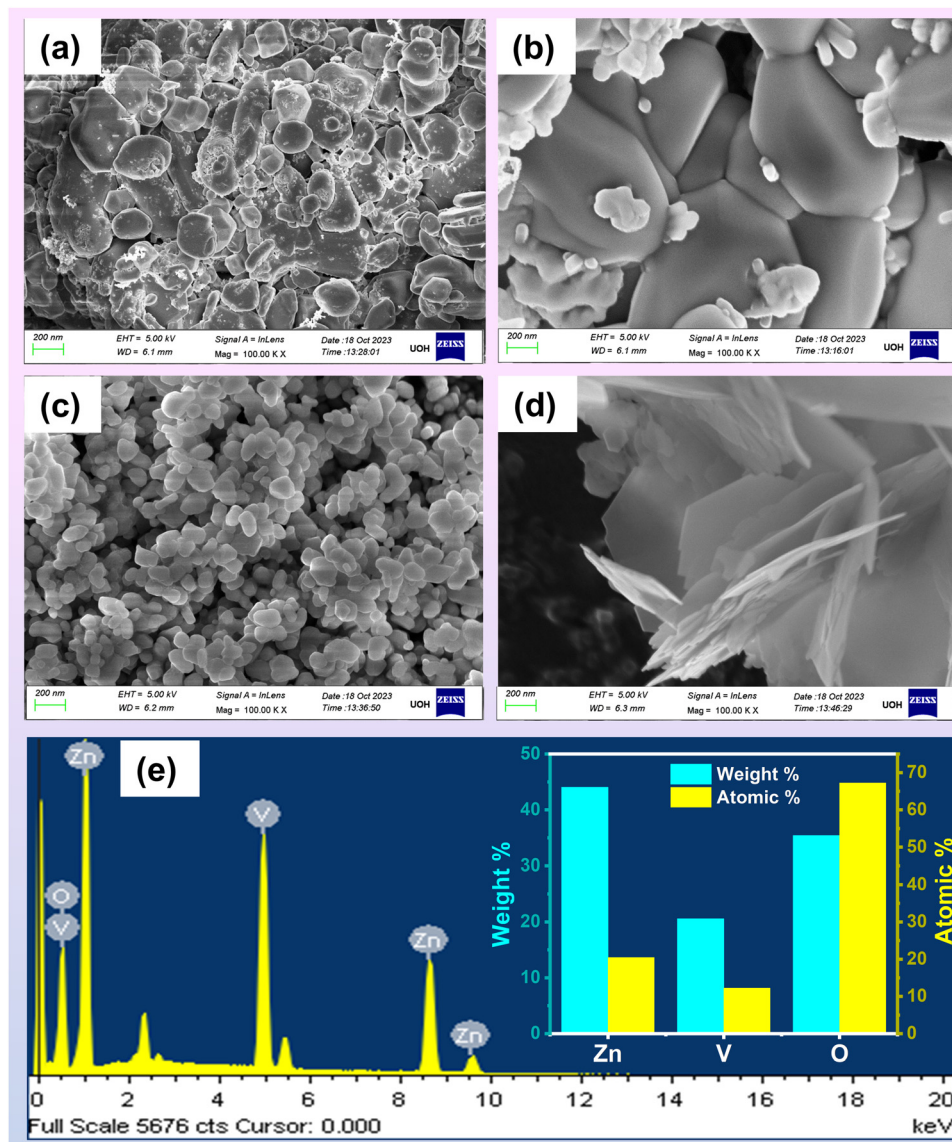| S. No.	Bond	Wavelength (cm^{-1})			
		SGM	UAC	CPM	HTM
1	Zn–O	413	417	420	426
2	V–O–Zn			549	449
3	V–O–V	620	620		
4	V–O–V	661	667	658	662
5	VO$_4$ corner atoms	791	788	793	789
6	V–O–V	843	850	843	848
7	V–O–V	900	917	901	907
8	V–O–V			966	
9	CH$_2$	1116	1110		
10	CH$_2$	1196	1189		1249
11	C=C	1627	1626	1623	1623
12	CH$_2$				2842
13	CH$_2$			2937	2921
14	H–O–H	3458	3454	3430	3410

Fig. 3 SEM micrographs of ZnVO NPs synthesized by different methods: (a) SGM, (b) UAC, (c) CPM, (d) HTM, and (e) EDAX data with insets showing atomic and weight percentages of CPM ZnVO NP.

atmospheric carbon dioxide. Additionally, several carboxylic and polymeric bands present in the unfired samples (Figure not shown) which disappears after high-temperature calcination.

3.1.3 Morphology. Fig. 3 illustrates the impact of various synthesis methods on the surface morphology and size of the ZnVO NPs. The SGM method yields irregularly shaped particles with sizes ranging from 200 to 500 nm, as shown in Fig. 3(a). The combustion method produces particles with irregular shapes and sizes varying from 100 to 600 nm, depicted in Fig. 3(b). In contrast, the CPM method results in spherical and elliptical particles with dimensions between 50 and 150 nm, as seen in Fig. 3(c). CPM is noted for its efficiency and cost-effectiveness, producing uniformly distributed particles with a porous microstructure beneficial for catalytic and LED applications. Fig. 3(d) shows that the HTM method results in flake-like morphology, with particles approximately 50–100 nm thick and

Table 2 Average particle size and morphology of ZnVO NPs synthesized by different methods, as observed from SEM images

S. No.	Synthesis method	Particle size	Particle shape
1	SGM	200–500 nm	Irregular
2	UAC	100–600 nm	Irregular
3	CPM	50–150 nm	Spherical
4	HTM	50–100 nm thickness	Flacks

100–300 nm wide. The SSM method, on the other hand, produces larger, rougher, pebble-like structures, as reported by previous studies.[25] The average particle sizes of the synthesized ZnVO samples, as determined from SEM images, are listed in Table 2. The EDAX spectrum of ZnVO NP confirms the presence of Zn, V, and O, with the atomic and weight percentages of CPM ZnVO NP shown in Fig. 3(e). This confirms

the purity of the synthesized ZnVO samples, though it also indicates a deficiency of oxygen, which is crucial for PL emission. Overall, these findings suggest that different synthesis methods can effectively control the morphology of ZnVO NP.

3.1.4 X-ray photoelectron spectroscopy. XPS was employed to analyze the composition and purity of the synthesized ZnVO CPM NPs. Fig. 4(a) displays the survey spectrum of ZnVO CPM NP, confirming the presence of zinc (Zn), oxygen (O), and vanadium (V) without detectable impurities. Fig. 4(b)–(d) presents the high-resolution spectra for Zn 2p, O 1s, and V 2p regions. In Fig. 4(b), the Zn 2p spectrum shows two pairs of peaks: Zn $2p_{1/2}$ at 1046.5 eV and Zn $2p_{3/2}$ at 1023.6 eV, corresponding to Zn^{2+} ions. Additionally, non-lattice Zn ions are observed at 1044.6 eV and 1021.4 eV. The binding energy difference between these pairs is 22.9 eV, closely matching the expected value of 22.97 eV. Fig. 4(c) shows the O 1s spectrum, deconvoluted into three bands at 529.9 eV, 531.3 eV, and 532.5 eV. The peak at 529.9 eV corresponds to lattice oxygen (O^{2-}) in the $Zn_3V_2O_8$ matrix. The higher binding energy at 531.3 eV is attributed to oxygen vacancies within the metal oxide matrix. The peak at 532.6 eV is associated with adsorbed hydroxyl groups (OH) or water (H_2O). The area ratios of these peaks 36.66%, 28.95%, and 34.39%, respectively indicate a notable concentration of oxygen vacancies, as supported by the EDAX data. Fig. 4(d) shows the V 2p spectra with two pairs of peaks: V $2p_{3/2}$ at 516.8 eV and 518.9 eV, and V $2p_{1/2}$ at 522.6 eV and 524.5 eV, corresponding to V^{4+} $2p_{1/2}$ and V^{5+} $2p_{1/2}$ states.[50,51] It is well-known that vanadium exhibits multiple oxidation states (V^{3+}, V^{4+}, and V^{5+}). In $Zn_3V_2O_8$, it primarily exists as V^{5+} within the $[VO_4]^{3-}$ tetrahedral units; however, partial reduction to V^{4+} can occur due to synthesis conditions, structural defects, or surface effects. Since XPS primarily probes the surface ($\sim$5–10 nm depth), high-temperature synthesis or post-processing can induce

partial reduction of V^{5+} to V^{4+} (VO_2-like states), resulting in detectable V^{4+} signatures in the XPS spectrum. Additionally, the presence of oxygen vacancies or Zn^{2+} substitution can alter the charge balance, stabilizing V^{4+} states within the lattice to maintain overall charge neutrality. Oxygen vacancies act as electron donors, facilitating charge compensation and contributing to the observed V^{4+} signal in the XPS spectrum. To confirm this, we performed a deconvolution of the V 2p XPS spectrum, presented in Fig. 4(d), where V^{4+} appears at a lower binding energy ($\sim$516.8 eV, V $2p_{3/2}$). Overall, the XRD, FTIR, FESEM, and XPS analyses confirm that the ZnVO CPM NPs are pure and free of impurities.

3.1.5 UV/vis-DRS analysis. Understanding absorption phenomena, excitation energy, and band gap is essential for investigating PL emission properties. The optical characteristics of ZnVO and the optical band gap energy (E_g) of the synthesized samples were analysed using UV/Vis-DRS spectroscopy. Fig. 5 displays the UV/Vis-DRS spectra of ZnVO nanostructures over a wavelength range of 200 to 900 nm. The reflectance peak observed between 350 and 400 nm is attributed to electronic transitions from O^{2-} to V^{5+} within the T_d VO_4 structure. The inset presents the optical E_g values of ZnVO, calculated using the Kubelka–Munk function and the Tauc plot, as described by eqn (9).[52–54]

$$(F(R_\infty)h\nu)^{1/n} = A(h\nu - E_g) \qquad (9)$$

where $F(R_\infty)$ is called the Kubelka–Munk function which is given in eqn (10),[55] which is the ratio of the absorption coefficient (k) to the scattering coefficient (s) in m^{-1}.

$$F(R_\infty) = \frac{(1 - R_\infty)^2}{2R_\infty} \qquad (10)$$

R_∞ is the % reflectance obtained in the DRS data, the subscript ∞ represents sufficient thickness specimen, $h\nu$ is the photon energy, E_g is the materials band gap and n depends on the type
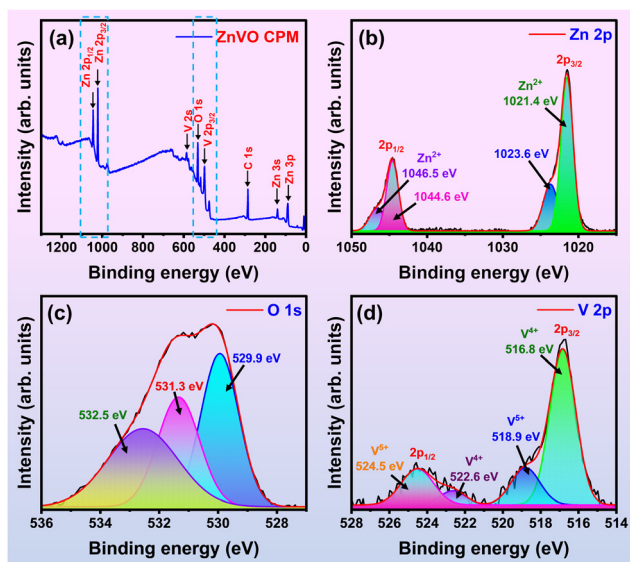

Fig. 4 XPS spectra of ZnVO NPs synthesized by the CPM method: (a) wide-range survey spectrum, (b) Zn 2p, (c) O 1s, and (d) V 2p energy regions.
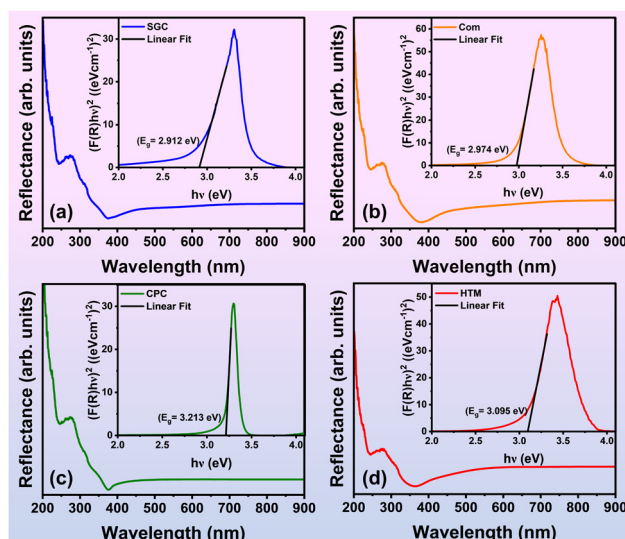

Fig. 5 UV/Vis-DRS spectra of ZnVO samples synthesized by different methods: (a) SGM, (b) UAC, (c) CPM, and (d) HTM. The inset shows the Kubelka–Munk function and Tauc plot for band gap estimation.

Table 3 Comparison of energy band gap values for ZnVO with other metal vanadates

S. No.	Samples	Energy band gap (E_g)	Ref.
1	$Zn_3V_2O_8$	2.68	56
2	CuV_2O_6	2.6	58
3	$BiVO_4$	2.5	59
4	$BiVO_4$	2.68	60
5	$Zn_3V_2O_8$	2.74	25
6	ZnVO-SGM	2.907	This work
7	ZnVO-UAC	2.970	This work
8	ZnVO-CPM	3.207	This work
9	ZnVO-HTM	3.090	This work

of ET ($\frac{1}{2}$ for direct and 2 for indirect bandgap). The sample E_g was calculated by projecting the linear component of the plots of $h\nu$ vs. $(F(R_\infty)h\nu)^2$ to the energy axis as shown in the inset of Fig. 5. The optical band gap energy (E_g) values for ZnVO samples synthesized by SGM, UAC, CPM, and HTM methods were determined to be 2.907 eV, 2.970 eV, 3.207 eV, and 3.090 eV, respectively. These values show an increase in the band gap with a decrease in particle size compared to previously reported data.[25] Variations in E_g can be attributed to differences in impurity levels, crystal size, and the nature of electronic transitions. The E_g values obtained in this study are consistent with previously reported values for vanadium-based metal oxides (E_g = 2.68).[25,56] As shown in Table 3, the E_g values achieved here are notably higher than those reported for other samples, attributed to cation substitution and the broader absorption range of ZnVO.[26] The observed small-range distortions, influenced by interactions among clusters, result in the formation of intermediate energy levels within the E_g of the phosphor, contributing to broadband emission. The minor variations in the E_g suggest that oxygen vacancies play a role in altering the band structure of the synthesized phosphors, as indicated by the observed shifts.[57]

3.2 Photoluminescence characterization

Fig. 6(a) and (b) present the PLE and PL spectra of ZnVO nanoparticles synthesized by various methods, measured at RT with an excitation wavelength of 361 nm. The spectra are consistent across all synthesis methods, indicating that similar excited centers are responsible for the broad PL emission observed. The larger FWHM of the emission spectra across different synthesis methods suggests that the $(VO_4)^{3-}$ groups are not uniformly distributed within the crystal lattice, which implies the presence of defect centers. These defects lead to a redistribution of energy levels in the conduction and valence bands, affecting the band gap and intrinsic emission properties. The PLE spectrum of ZnVO nanoparticles results from the CT of an electron from the 2p orbital of oxygen to the unoccupied 3d orbital of vanadate ions in VO_4 with T_d symmetry.[25,61–63] The PL spectra exhibit significant visible light emission spanning from 440 to 740 nm, with broadband emission peaks centered at 573 nm (SGM), 572 nm (UAC), 562 nm (CPM), 572 nm (HTM), and 575 nm (SSM). This broad emission is attributed to the self-trapped excitation radiative recombination process.

The PLE spectrum of ZnVO NP is because of the CT of an electron from 2p orbital (O) to the unoccupied 3d orbital (vanadate) ions in VO_4 with T_d symmetry.[25,61–63] The PL spectrum features two prominent peaks corresponding to emission from the higher energy $^3T_2$ and $^3T_1$ states to the ground $^1A_1$ state of the V^{5+} ion. The intensity of the PL spectrum is notably higher, indicating efficient recombination of electrons and holes. Among the synthesized samples, those produced via the CPM method exhibit the highest PL intensity, followed by SSM, HTM, UAC, and SGM. Despite the consistent phase observed in all synthesis routes according to XRD (Fig. 1), the samples show significantly different morphologies. The PL emission in ZnVO nanoparticles is strongly influenced by particle size, oxygen vacancies, and the material's morphology. The observed PL band originates from defect states, as confirmed by FESEM and XPS analyses, which introduce intermediate energy levels within the band gap.

The photoluminescence (PL) characteristics of self-activated $Zn_3V_2O_8$ originate from the intrinsic luminescent centers associated with the $[VO_4]^{3-}$ tetrahedral units, which act as primary emission centers. Upon excitation, charge transfer occurs via the ligand-to-metal charge transfer (LMCT) mechanism, where electrons are promoted from the O 2p orbitals of the oxygen ligands to the empty V 3d orbitals of vanadium. This oxygen-to-vanadium charge transfer ($O^{2-} \rightarrow V^{5+}$) results in a broad emission band, typically in the blue-green spectral region, attributed to the relaxation of excited electrons back to the ground state through radiative recombination. The presence of V^{4+} states due to surface defects, oxygen vacancies, or Zn^{2+} site substitution can introduce intermediate energy levels within the band gap, facilitating additional recombination pathways and modifying the emission profile. Moreover, the phonon-assisted relaxation process plays a critical role in spectral broadening, as energy dissipation through lattice vibrations can further modulate the emission characteristics. The intensity and position of the PL emission are strongly influenced by crystal field strength, structural distortions, and synthesis conditions, which dictate the extent of electronic delocalization and defect-related emission processes. The CPM-synthesized samples demonstrate the highest PL intensity, likely due to their spherical morphology and uniform particle size compared to those synthesized by SGM, UAC, HTM, and SSM. Accumulation of defects and additional oxygen vacancies lead to a higher number of inactive V^{4+} units, which contribute less to charge transfer and emission from V^{5+}, thereby broadening the emission band and enhancing PL intensity. This occurs because the defects and oxygen vacancies alter the material's electronic structure, creating additional radiative recombination pathways that increase the PL intensity.

Although the charge transfer efficiency is reduced, the overall PL intensity is enhanced due to the increased number of radiative recombination pathways. As a result, the emission band broadens, and the PL intensity increases, indicating a complex interplay between defects, oxygen vacancies, and the material's optical properties. By tailoring the defect density, doping strategies, or nanostructuring, the luminescence
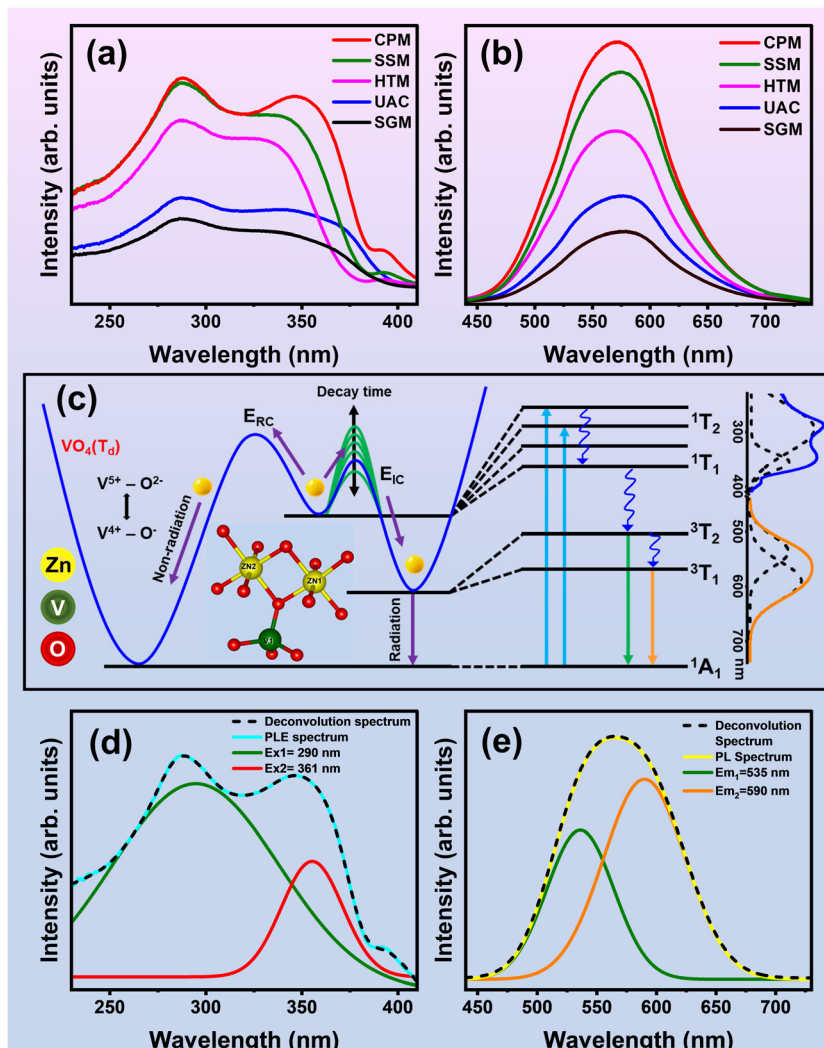
Fig. 6 Photoluminescence analysis of ZnVO samples. (a) Photoluminescence excitation (PLE) spectra, (b) photoluminescence (PL) emission spectra for ZnVO synthesized *via* SGM, UAC, CPM, and HTM methods, compared to the SSM sample, (c) schematic energy level diagram, (d) deconvoluted excitation spectrum, (e) deconvoluted emission spectra of ZnVO NPs synthesized by the CPM method.

efficiency of $Zn_3V_2O_8$ can be fine-tuned for advanced solid-state lighting and optoelectronic applications.

The schematic model in Fig. 6(c) provides a clear representation of the energy diagram and transition states of ZnVO NPs during luminescence. It depicts the two primary relaxation mechanisms for an excited electron: nonradiative recombination and radiative processes. The excited electron, illustrated as a yellow ball, follows the paths indicated by the purple arrows. The green arc represents fluctuations in decay time due to the dynamic Jahn–Teller effect a time-dependent distortion of the VO_4 tetrahedron. The blue curve illustrates the relative energy of the VO_4 tetrahedra. The optical characteristics of phosphors are primarily determined by the luminescence center, but the coordination environment and local geometry also play significant roles. For the V^{5+} ion with T_d symmetry, the molecular orbitals include one ground state ($^1A_1$) and four excited states $^1T_1$, $^1T_2$, $^3T_1$, and $^3T_2$.[25,61–63]

In the CPM-synthesized samples, the absorption band at 290 nm in the excitation spectrum corresponds to the $^1A_1 \rightarrow$ $^1T_2$ transition, while the excitation at 361 nm is attributed to the partially permitted $^1A_1 \rightarrow$ $^1T_1$ transition. The Gaussian deconvolution of the excitation spectra reveals two bands associated with these transitions. The ZnVO NPs synthesized *via* the CPM method exhibit a broadband excitation spectrum spanning 220 to 410 nm, with peaks at 290 nm (Ex_1) and 361 nm (Ex_2), and a smaller peak at approximately 385 nm (Fig. 6(d)). These absorption bands result from a partially permitted spin-forbidden transition in the T_d symmetry of VO_4^{3-}. The charge transfer (CT) of an electron from O^{2-} to V^{5+} ions (from the 2p to the 3d orbital) in the VO_4^{3-} group is confirmed to cause the broad emission of vanadate phosphors.

The emission spectrum of the ZnVO NPs, deconvoluted into two bands, corresponds to the energy transfers (ETs) from $^3T_1$ and $^3T_2 \rightarrow$ $^1A_1$. These transitions are influenced by spin–orbital

interactions in the defect structure (Fig. 6(e)). The FWHM values of 66 nm and 80 nm for the Em_1 and Em_2 bands indicate that the broadness of the PLE spectrum has increased along with its intensity. Additionally, the reduction in the crystallite size of the ZnVO NPs may contribute to the observed blue shift. The size, shape, and crystallinity of the phosphor particles significantly affect their luminous capabilities. We propose that the CT transitions from the $^3T_2$ and $^3T_1$ states to the $^1A_1$ state play a crucial role in enhancing the peak intensity of the Em_1 and Em_2 bands.

3.3 Quantum yield, colorimetric properties, and decay measurements

The absolute QY of ZnVO samples, measured under 361 nm excitation, was found to be 20%, 31%, 74%, and 49% for SGM, UAC, CPM, and HTM methods, respectively, as shown in Fig. 7(a). The higher QY of the CPM sample compared to SGM, UAC, HTM, and previously reported SSM[19] is attributed to enhanced excitation diffusion, facilitated by the hybridization of the Zn 3d and O 2p orbitals in the lower energy band, and the Zn 4s and V 3d orbitals in the higher energy band.[42] While commercial phosphors such as $Y_3Al_5O_{12}:Ce^{3+}$ (70–90%),[64] $La_3Si_6N_{11}:Ce^{3+}$ (85%),[65] $(Sr, Ba)_2SiO_4:Eu^{2+}$ (80%),[66] $Lu_3Al_5O_{12}:Ce^{3+}$ (74%),[67] $BaMgAl_{10}O_{17}:Eu^{2+}$ (91%),[68] exhibit QYs over 80%, the ZnVO CPM nanoparticles achieved a remarkable 74% efficiency under 361 nm excitation. This value is comparable to rare-earth-doped commercial phosphors and previously reported vanadate-based phosphors, as shown in ESI,† Table S3. When compared to commercial phosphors such as $(Sr,Ca)AlSiN_3:Eu^{3+}$ ($2.6 \times 10^3 \text{ cm}^{-1}$)[69] and $(Ba,Sr)_2SiO_4:Eu^{2+}$ ($3.2 \times 10^3 \text{ cm}^{-1}$),[66] the Stokes shift (ΔS) of the ZnVO (CPM) NPs is significantly higher at $9.9 \times 10^3 \text{ cm}^{-1}$, as seen in Fig. 7(b). This higher ΔS value enables these phosphors to emit white light with improved CRI and reduced glare, making them ideal for indoor lighting applications. Therefore, ZnVO nanoparticles synthesized by the CPM method are well-suited for UV-based WLEDs with high CRI and LE, owing to their higher ΔS value and enhanced red emission. Fig. 7(c) displays the Commission Internationale de l'Éclairage (CIE) color coordinates of ZnVO CPM samples, under black light irradiation, at (0.43, 0.52). The emission color of phosphors synthesized using different methods varied slightly, as indicated by (x, y) values of (0.44, 0.51), (0.44, 0.51), and (0.42, 0.52) for the SGM, UAC, and HTM samples, respectively, as shown in ESI,† Fig. S1. In ZnVO nanoparticles, excitation with optimal T_d symmetry is allowed through the $^1A_1 \rightarrow {}^1T_1$ and $^1A_1 \rightarrow {}^1T_2$ transitions. However, the intersystem crossing transitions ($^1T_1$, $^1T_2 \rightarrow {}^3T_1$, $^3T_2$) and the forbidden $^3T_1$, $^3T_2 \rightarrow {}^1A_1$ transition, due to the spin selection rule, also play a role in determining the observed luminescence.[25,61–63]

The decay profile was analyzed to understand the mechanism behind the broad emission and its dependence on excitation wavelength, temperature, and emission. When the synthesized CPM nanoparticles were excited at UV wavelengths (290 nm and 361 nm), the emission intensity increased, reaching a maximum at 361 nm, and then decreased at higher
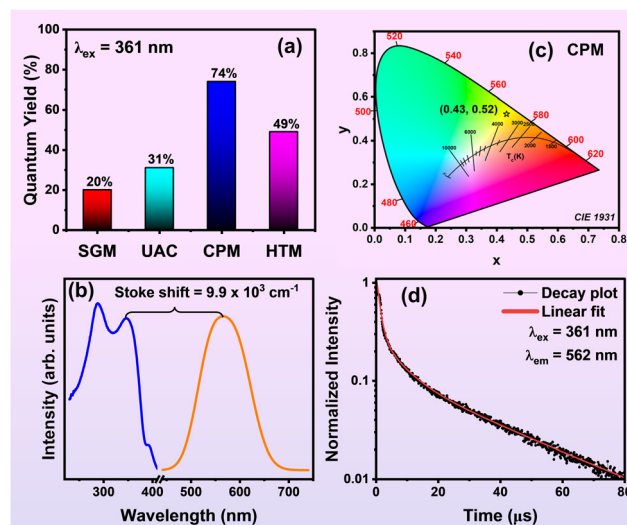

Fig. 7 (a) Quantum yield of ZnVO synthesized *via* SGM, UAC, CPM, and HTM methods under 361 nm excitation wavelength, (b) Stokes shift, (c) CIE color coordinates, and (d) Decay curves under 361 nm excitation and 562 nm emission for ZnVO CPM NPs.

excitation wavelengths (385 nm), as shown in ESI,† Fig. S2. The UV-vis spectrum confirms that the highest excitation maxima occur at 361 nm, which also corresponds to the second maximum emission intensity, attributed to bandgap energy absorption. At higher excitation wavelengths (385 nm), defect states contribute more significantly to the emissions, leading to a shift and an increase in the full width at half maximum (FWHM). The luminescence decay curves of ZnVO nanoparticles, observed with an excitation wavelength of 361 nm and an emission wavelength of 562 nm, are shown in Fig. 7(d). The extended lifetime in the microsecond range suggests that the emission originates from the excited triplet state. This indicates the involvement of a slow, radiative recombination process, likely influenced by the presence of defect states, contributing to the overall broad emission. The decay lifetime values obtained using eqn (11), individual lifetime, and contribution population are found to be 19%, 59%, and 22% for τ_1, τ_2, and τ_3[70,71]

$$I = I_0 + A_1 \exp\left(\frac{-t}{\tau_1}\right) + A_2 \exp\left(\frac{-t}{\tau_2}\right) + A_3 \exp\left(\frac{-t}{\tau_3}\right) \quad (11)$$

where t is the decay lifetime, $I(t)$ is the intensity at time t, I_0 is the starting PL intensity, A_1, A_2 and A_3 are the fit coefficient and τ_1, τ_2 and τ_3 are the life time component, respectively. This triexponential fitting is obtained because of the activation energy level other than the two triplet excited levels, such as oxygen vacancy level, which contributes to lifetime decay. The average decay times for ZnVO NPs are calculated using the eqn (12).[71–74]

$$\tau_{avg} = \frac{A_1\tau_1^2 + A_2\tau_2^2 + A_3\tau_3^2}{A_1\tau_1 + A_2\tau_2 + A_3\tau_3} \quad (12)$$

The average lifetime of CPM-synthesized ZnVO nanoparticles is found to be 23.06 μs. This indicates that the lifetime

decreases as the concentration of defect states increases, leading to more non-radiative relaxation pathways, transitioning from bulk to nanoscale, as confirmed by XPS analysis. Fig. 6(e) shows that an increase in oxygen vacancy density results in enhanced red emission while blue-green emission diminishes. Therefore, ZnVO nanoparticles, with their microsecond decay time, are highly suitable for WLED applications, comparable to the decay period of YAG:Ce^{3+} as reported by Guan *et al.*[75] This suggests that in the ZnVO lattice, emission is primarily driven by the VO_4^{3-} luminescent center. Moreover, ZnVO nanoparticles act as single-emitting-center phosphors, and materials with shorter decay times are ideal for use in WLEDs.

3.4 Thermal quenching properties and irradiation time PL

One of the critical factors affecting both the lifespan and performance of WLEDs, as well as the color stability of the emitted light, is the thermal stability of the phosphor.[66,76] To ensure that the thermal quenching behavior of ZnVO NPs (CPM) aligns with the perating temperatures of WLEDs, we conducted temperature-dependent studies on the ZnVO NPs. In the liquid phase, molecules experience various motions—collisions, rotations, vibrations, and translations—which intensify when thermal energy is applied, leading to energy loss. However, in the solid state, where intermolecular and translational rotational motions are restricted, thermal quenching occurs less frequently. As the temperature increases, we observe a linear decrease in emission intensity from the ZnVO NPs in the solid state, from 25 °C to 275 °C, as shown in Fig. 8(a). The decline in PL intensity with increasing temperature is attributed to vibrational energy loss of excited electrons. A blue shift was noted with rising temperature, possibly due to the acceleration of non-radiative relaxation processes, defect-mediated emission, or predominated CT emission. The emission

intensity of ZnVO CPM NPs retained 89% of its value at 150 °C and 78% at 275 °C, indicating excellent thermal stability. At RT, electrons are excited from the ground state $^1A_1 \rightarrow {}^3T_2$ state before returning to $^1A_1$. However, at higher temperatures, the emission decreases as electrons transition directly from $^1A_1$ to the $^1T_2$ state, bypassing the $^3T_1$ state. As temperature increases, the excitation energy is transferred from the luminescent core to non-radiative thermal energy through lattice relaxation. This relaxation process results in a reduction of PL intensity due to non-radiative transitions, which manifest as a Stokes shift.[77] Thermal quenching was observed at 180 °C for ZnVO NPs, slightly lower than the ZnVO bulk material, likely due to the larger Stokes shift. Despite a minor reduction in PL intensity, ZnVO NPs exhibit strong thermal stability and can be utilized at temperatures up to 210 °C, making them suitable for high-temperature applications in WLEDs. The Arrhenius equation was used to determine the activation energy (ΔE) for both phosphors to support the thermal quenching phenomenon as shown in eqn (13).[25,73,74]

$$I_T = \frac{I_0}{1 + c \exp\left(\dfrac{\Delta E}{kT}\right)} \quad (13)$$

Here, c is a constant, I_0 and I_T are the initial and various temperatures of PL intensity, and k is the Boltzmann constant in eV, respectively. Fig. 8(b) shows the relationship between $\ln[(I_0/I_T) - 1]$ and $1/(kT)$ for ZnVO NPs. The slope of the linear plot was used to calculate the activation energy, which was found to be approximately 0.158 eV for ZnVO NPs. The results indicate that as the Stokes shift increases, the ΔE decreases, leading to thermal quenching of ZnVO NPs at lower temperatures. Typically, a lower ΔE value increases the likelihood of nonradiative energy transfer. However, the ΔE value of ZnVO NPs synthesized *via* CPM (~0.158 eV) is comparable to that of ZnVO synthesized by SSM (0.163 eV). UV-Vis and XPS analyses revealed a reduction in bandgap values and a rise in the valence band position, suggesting a shift in the band structure caused by increasing defect states. These changes reduce the distance between the luminescence center and the crossover point, resulting in a lower activation energy for quenching. The enhancement of the thermal quenching effect is attributed to the creation of trapping levels between the lowest excited level curve of VO_4^{3-} ($^3T_1$) and the ground state curve of the VO_4^{3-} group ($^1A_1$). This makes ZnVO NPs suitable for the production of WLEDs, where high thermal stability is essential for ensuring a long operating lifespan and higher LE. Additionally, the photostability of ZnVO NPs was evaluated over 4 hours of 361 nm illumination. As shown in Fig. 8(c) and (d), the normalized PL spectra remained unchanged in terms of both spectral position and intensity, even after extended irradiation at room temperature (RT) and elevated temperatures (150 °C). A comparison of the normalized PL emission intensity *versus* irradiation time (ESI,† Fig. S3a and b) at RT and 150 °C shows that after 4 hours of continuous exposure, the emission intensities remained at 99.46% at RT and 99.11% at 150 °C of their initial
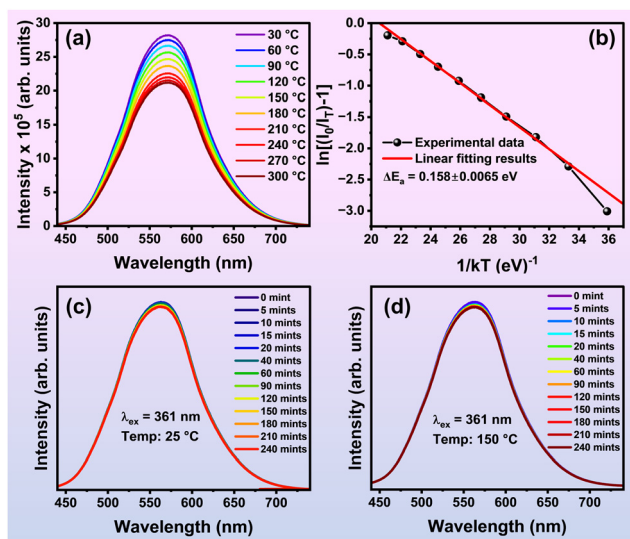

Fig. 8 (a) Solid-state temperature-dependent PL spectra, (b) activation energy graphs fitted using the Arrhenius equation, and PL spectra as a function of irradiation time under 361 nm excitation at (c) room temperature and (d) elevated temperature (150 °C).

values. Thus, extended irradiation and elevated temperatures do not significantly affect the stability of ZnVO NPs, highlighting their robust photostability.

3.5 Application in WLEDs and colorimetric calculations

A WLED prototype was created by combining ZnVO CPM NPs with epoxy resin and a 385 nm, 0.5 WLED chip. Fig. 9(a(i)) illustrates the schematic of the ZnVO CPM NP LED package before applying current. Upon applying a current of ∼150 mA, the LED emitted a pleasant white light, as seen in Fig. 9(a(ii)). The LED produced a sharp peak at 385 nm, while the ZnVO CPM NPs generated a broad visible spectrum ranging from 400–800 nm, as shown in Fig. 9(b). The CIE color coordinates of the white emission from the ZnVO CPM NPs are (0.330, 0.301), close to ideal white light, with a CCT of ∼4920 K, outperforming YAG: Ce^{3+}-based WLEDs, which typically have a CCT around 6500 K.[78] The superior color quality of the ZnVO CPM NP and LED prototypes is highlighted in the CIE 1931 chromaticity diagram (Fig. 9(c)), where the CIE coordinates of the ZnVO CPM NP emission, excited at 385 nm, are plotted. The coordinates (0.330, 0.301) are close to the optimal white light equal energy point (0.333, 0.333), demonstrating excellent cool white light properties. It is noteworthy that the commercial YAG: Ce^{3+} phosphor, developed by Wolf Speed, Inc., exhibits a QY of 78% at 449 nm excitation. When compared to P-20 (LUMINOX), bulk YAG: Ce^{3+} (CREE), and bulk ZnVO, the ZnVO CPM NP shows similar or superior performance.[79] Table 4 outlines the relative efficiency of these bulk phosphors and ZnVO CPM NPs at various excitation wavelengths. The QY of ZnVO CPM NPs is comparable to these bulk phosphors and represents a significant improvement over the commonly used yellow-lighting P-20 phosphor. Further reduction of particle size into the quantum

Table 4 Comparison of relative quantum yield (QY) for ZnVO-CPM NP with bulk phosphors (YAG: Ce^{3+},P-20,$Zn_3V_2O_8$) and CIE color coordinates of ideal white light, ZnVO-CPM NP, and the simulated white light produced using ZnVO-CPM NP and LED

Company name	Product name	λ_{ex}	QY (%)
CREE	YAG: Ce^{3+}	449	78
CREE	YAG: Ce^{3+}	385	58
LUMINOX	P-20	385	51
$Zn_3V_2O_8$-bulk	ZnVO	385	68
$Zn_3V_2O_8$-NP	ZnVO-CPM	385	76
Sample		CIE (x, y)	
IDEAL white		(0.333, 0.333)	
ZnVO-CPM NP		(0.432, 0.522)	
385 nm LED + ZnVO-CPM NP (white light)		(0.330, 0.301)	

range could enhance the QY even more, as Bhargava *et al.*[80] demonstrated for various NP systems. Fig. 9(d) presents the PL spectra for yellow-emitting P-20, bulk $Zn_3V_2O_8$ phosphor, YAG: Ce^{3+}, and ZnVO CPM NPs. The CIE color coordinates for the ideal white light, the 385 nm LED, ZnVO CPM NP, and the simulated white light (combining the 385 nm LED with ZnVO CPM NP) are listed in Table 4. These coordinates, derived using the equal-wavelength method,[81] are crucial for determining the precise emission color of each sample, as visualized in the CIE chromaticity diagram.[81]

We are pleased to report that the WLED exhibited outstanding EL performance at a driving voltage of 3 V, producing cool white light with a CCT of 4920 K. Fig. 10(a) and the fabricated device shown in ESI† (Fig. S4) show images of the setup: (i) a 385 nm LED chip and a glass slide coated with ZnVO/epoxy resin, (ii) and (iii) the white light emission
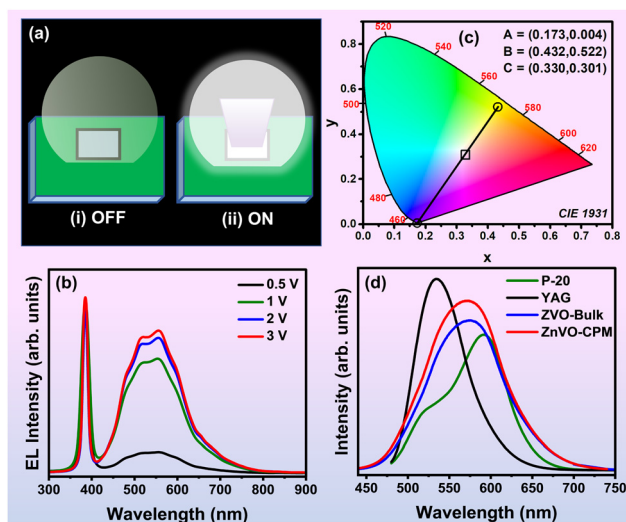

Fig. 9 (a) Schematic diagram of an LED chip coated with ZnVO-CPM NPs, shown (i) before applying current and (ii) after applying current. (b) Electroluminescence (EL) spectrum of a WLED excited at 385 nm under different applied voltages (0.5 V, 1 V, 2 V, and 3 V). (c) CIE chromaticity diagram. (d) Comparison of PL spectra for commercial P-20 (LUMINOX), YAG: Ce^{3+} (CREE), ZnVO bulk phosphor, and ZnVO-CPM NPs.
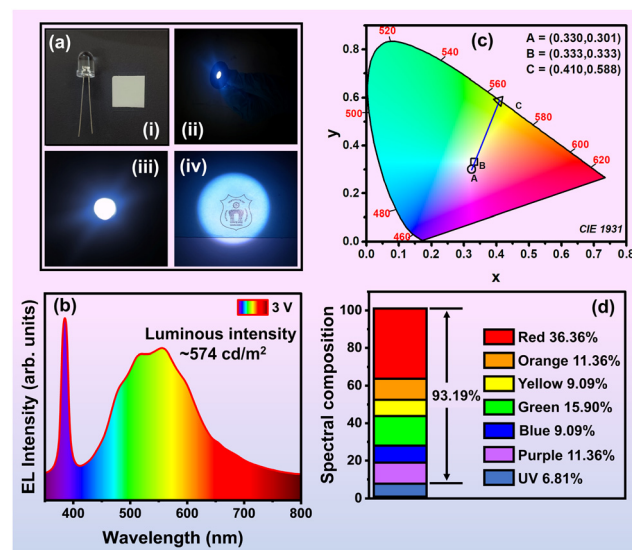

Fig. 10 (a) Images showing (i) a 385 nm LED chip and a glass slide coated with ZnVO/epoxy resin, (ii) side view of the white light emission, (iii) top view of the white light emission, and (iv) the NITW logo illuminated by the white light emitted from the ZnVO-coated 385 nm LED at 3 V. (b) CIE color coordinates of the white light emission. (c) Electroluminescence (EL) spectrum of the WLED. (d) Spectral composition of the fabricated WLED, excited by the 385 nm LED chip and ZnVO CPM NP.

from the side and top views of the LED device, and (iv) the NIT Warangal (NITW) logo illuminated by the ZnVO and 385 nm LED at 3 V. The device's effective emission of polychromatic light upon excitation with 385 nm radiation confirms the ZnVO CPM NP's efficiency. The luminous value of the WLED device fabricated using our synthesized $Zn_3V_2O_8$ phosphor is quite promising, with a luminous intensity of ~ 574 cd m^{-2}. This suggests that our material has good potential for application in solid-state lighting devices. Fig. 10(b) illustrates the spectral output from 360 nm to 800 nm for the WLED, combining a 385 nm LED with ZnVO CPM NP at 3 V. The resulting spectrum aligns closely with the "ideal white" region on the CIE chromaticity diagram, shown in Fig. 10(c). This suggests that ZnVO CPM NP is highly effective in converting 385 nm LED light into white light. The color temperature of a Planckian blackbody radiator with a similar white light color is used to define the CCT, highlighting the potential of ZnVO CPM NP for high-quality white light LED applications.[82] The McCamy determined the value of CCT,[83,84] using the following eqn (14):

$$CCT = -499n^3 + 3525n^2 - 6823.3n + 5520.33 \quad (14)$$

where $n = (x_{ee} - x)/(y_{ee} - y)$ and the epicenter is at $x = 0.330$, $y = 0.301$, (x_{ee}, y_{ee}) is the equal energy point. The synthesized ZnVO CPM NP exhibited a CCT of approximately 4920 K, placing it firmly in the cool white light region. A higher CCT value generally indicates improved visual perception and brightness.[85] Given that the CCT of ZnVO CPM NP falls within the cool white light range, it is well-suited for use in WLEDs for everyday illumination. As shown in Fig. 10(d), the spectrum includes about 93.18% visible light, with a significant proportion of red components ($\sim 36.36\%$), making it an excellent choice for comfortable indoor lighting, including reading. To assess color purity, the distance between the emitted color coordinates and the equal energy point on the CIE diagram is compared to the distance between the equal energy point and the dominant wavelength point. This method helps determine the purity of the dominant color in the test source. Using eqn (15), the color purity[25] of ZnVO CPM NP was determined.

$$\text{Color purity} = \frac{\sqrt{(x - x_{ee})^2 + (y - y_{ee})^2}}{\sqrt{(x_d - x_{ee})^2 + (y_d - y_{ee})^2}} \quad (15)$$

where (x_{ee}, y_{ee}) is the equal energy point reference illuminate, (x_d, y_d) is the dominant wavelength point, and (x, y) is the CIE coordinates of the light source under test, respectively.[63] The computed color purity for the CIE coordinates excited at 385 nm is 0.12065. Lower color purity values indicate better white light emission, making the ZnVO CPM NPs a promising candidate for WLEDs when used with a NUV LED chip. The CCT values of the ZnVO CPM NPs are well within the cool white light range, making them suitable for general lighting applications. A notable finding is that all EL parameters, including CRI, CIE color coordinates, and CCT, remained stable across various driving voltages (0.5 to 3 V) as detailed in ESI† (Table S4). The device maintained high performance during extended operation times with minimal changes in EL, as shown in ESI† (Fig. S5a) and ESI† (Tables S5 and S6). The EL stability under different temperatures was thoroughly evaluated, with the device showing consistent performance across a range of temperatures, as demonstrated in ESI† (Fig. S5b). Crucially, all EL parameters, including CRI, CIE coordinates, and CCT values, remained stable across temperature tests, with no significant changes in CIE color coordinates, CCT values staying below 4853 K, and CRI values consistently above 85. These results highlight the excellent performance and potential practical applications of the ZnVO CPM NP-based WLEDs.

4. Conclusions

$Zn_3V_2O_8$ nanophosphors were successfully synthesized using the coprecipitation calcination method. These vanadate phosphors exhibited broad emission from 400 nm to over 750 nm due to charge transfer transitions in VO_4 tetrahedra, with a yellow emission and CIE color coordinates of (0.43, 0.52). Among the synthesis methods, the coprecipitation method produced ZnVO NPs with the highest quantum yield, in the order of CPM > HTM > UAC > SGM, with corresponding values of 74%, 49%, 31%, and 20%. The ZnVO NPs displayed a broad yellow emission centered at 562 nm upon excitation at 361 nm, with FWHM values of 66 nm for Em_1 and 80 nm for Em_2. The thermal stability of the ZnVO NPs was demonstrated by their retention of 78% of room temperature emission at 275 °C and an activation energy (ΔE) of ~ 0.158 eV. When integrated with a 385 nm LED chip, the ZnVO NPs achieved a cool CCT of ~ 4920 K, a high CRI of 91%, and CIE coordinates of (0.330, 0.301). This work presents a cost-effective, rare earth-free, self-activated approach to enhancing vanadate phosphors for WLED applications. The WLEDs exhibited stability across various currents, operating times, and temperatures, maintaining their electroluminescence, CCT, CIE coordinates, and CRI values.

Author contributions

M. Rakshita: data curing, methodology, writing – original draft. Aachal A. Sharma: data curation; investigation. Payal P. Pradhan: data curation; investigation. K. A. K. Durga Prasad: data curation; investigation. M. Srinivas: data curation, formal analysis. D. Haranath: conceptualization; funding acquisition; methodology; supervision; writing – review & editing.

Data availability

The data that support the findings of this study are available from the corresponding author upon reasonable request.

Conflicts of interest

The authors declare that they have no known competing financial interests or personal relationships that could have appeared to influence the work reported in this paper.

Acknowledgements

Notes and references

1 K. Jayanthi Rajan and S. V. Manorama, Formation of hierarchical macro porous YAlO:Ce multifunctional nanophosphors, *J. Appl. Phys.*, 2016, **119**, 114902, DOI: **10.1063/1.4943418**.

2 R. Verstraete, H. F. Sijbom, J. J. Joos, K. Korthout, D. Poelman, C. Detavernier and P. F. Smet, Red Mn^{4+}-Doped Fluoride Phosphors: Why Purity Matters, *ACS Appl. Mater. Interfaces*, 2018, **10**, 18845–18856, DOI: **10.1021/acsami.8b01269**.

3 P. Botella, F. Enrichi, A. Vomiero, J. E. Munõz-Santiuste, A. B. Garg, A. Arvind, F. J. Manjón, A. Segura and D. Errandonea, Investigation on the Luminescence Properties of $InMO_4$ (M = V^{5+}, Nb^{5+}, Ta^{5+}) Crystals Doped with Tb^{3+} or Yb^{3+} Rare Earth Ions, *ACS Omega*, 2020, **5**, 2148–2158, DOI: **10.1021/acsomega.9b02862**.

4 S. Elleuch, A. Lusson, S. Pillet, K. Boukheddaden and Y. Abid, White Light Emission from a Zero-Dimensional Lead Chloride Hybrid Material, *ACS Photonics*, 2020, **7**, 1178–1187, DOI: **10.1021/acsphotonics.9b01817**.

5 S. Hu, C. Lu, G. Zhou, X. Liu, X. Qin, G. Liu, S. Wang and Z. Xu, Transparent YAG:Ce ceramics for WLEDs with high CRI:Ce^{3+} concentration and sample thickness effects, *Ceram. Int.*, 2016, **42**, 6935–6941, DOI: **10.1016/j.ceramint.2016.01.079**.

6 Y. Zhang, L. Li, X. Zhang and Q. Xi, Temperature effects on photoluminescence of YAG:Ce^{3+} phosphor and performance in white light-emitting diodes, *J. Rare Earths*, 2008, **26**, 446–449, DOI: **10.1016/S1002-0721(08)60115-5**.

7 Y. Wan, P. Dang, D. Liu, Q. Zhang, Y. Wei, H. Lian, G. Li and J. Lin, Highly Efficient Narrow-Band Green-Emitting Na_3K_5-$(Li_3SiO_4)_8$:Eu^{2+} Phosphor with Low Thermal Quenching, *Chem. Mater.*, 2023, **5**, 10702–10712, DOI: **10.1021/acs.chemmater.3c02579**.

8 M. Cai, T. Lang, T. Han, D. Valiev, S. Fang, C. Guo, S. He, L. Peng, S. Cao, B. Liu, L. Du, Y. Zhong and E. Polisadova, Novel Cyan-Green-Emitting Bi^{3+}-Doped $BaScO_2F$, R^+ (R = Na, K, Rb) Perovskite Used for Achieving Full-Visible-Spectrum LED Lighting, *Inorg. Chem.*, 2021, **60**, 15519–15528, DOI: **10.1021/acs.inorgchem.1c02150**.

9 Y. Lin, G.-E. Wang, L. Li, C.-L. Hu, S. Lin and J.-G. Mao, Rare-Earth-Free Barium Borostannate with Deep-Blue Light Emission, *Chem. Mater.*, 2021, **33**, 1852–1859.

10 E. Pavitra, G. Seeta Rama Raju, L. Krishna Bharat, J. Y. Park, C. H. Kwak, J. W. Chung, Y. K. Han and Y. S. Huh, Evolution of highly efficient rare-earth free $Cs_{(1−x)}Rb_xVO_3$ phosphors as a single emitting component for NUV-based white LEDs, *J. Mater. Chem. C*, 2018, **6**, 12746–12757, DOI: **10.1039/c8tc05110k**.

11 Y. Li, B. Yu, H. Wang and Y. Wang, Structural and optical characteristics of novel rare-earth-free red-emitting $BaSn(PO_4)_2$:Mn^{4+} phosphor, *J. Mol. Struct.*, 2021, **1229**, 129839, DOI: **10.1016/j.molstruc.2020.129839**.

12 M. K. Jang, Y. S. Cho and Y. D. Huh, Preparation of red-emitting $BaSiF_6$:Mn^{4+} phosphors for three-band white LEDs, *Opt. Mater.*, 2020, **101**, 109734, DOI: **10.1016/j.optmat.2020.109734**.

13 R. Cao, X. Ceng, J. Huang, X. Xia, S. Guo and J. Fu, A double-perovskite Sr_2ZnWO_6:Mn^{4+} deep red phosphor: synthesis and luminescence properties, *Ceram. Int.*, 2016, **42**, 16817–16821, DOI: **10.1016/j.ceramint.2016.07.173**.

14 A. A. G. Santiago, M. C. Oliveira, R. A. P. Ribeiro, R. L. Tranquilin, E. Longo, S. R. De Lázaro, F. V. Motta and M. R. D. Bomio, Atomistic Perspective on the Intrinsic White-Light Photoluminescence of Rare-Earth Free $MgMoO_4$ Nanoparticles, *Cryst. Growth Des.*, 2020, **20**, 6592–6603, DOI: **10.1021/acs.cgd.0c00757**.

15 A. A. Sharma, A. O. Chauhan, C. B. Palan and S. K. Omanwar, Synthesis and Photoluminescence study of Gd^{3+} doped YP_3O_9 phosphor prepared by Citric sol–gel method, *IJRST*, 2021, **8**, 65–69.

16 R. Muniramaiah, G. Maharana, J. M. Fernandes, M. Manivel Raja, D. B. Padmanaban, P. Supraja, M. Rakshita, N. P. Reddy, M. Kovendhan, G. Laxminarayana, R. R. Kumar, D. Haranath and D. P. Joseph, Sputter-deposited highly flexible noble metal multi-layer electrode viable for energy and luminescent devices, *Surf. Interfaces*, 2023, **39**, 102949, DOI: **10.1016/j.surfin.2023.102949**.

17 R. Muniramaiah, J. M. Fernandes, M. M. Raja, D. B. Padmanaban, P. Supraja, M. Rakshita, N. P. Reddy, G. Maharana, M. Kovendhan, G. Veerappan, G. Laxminarayana, R. R. Kumar, D. Haranath and D. P. Joseph, Mechanically stable ultrathin flexible metallic Au/Pt/Au tri-layer as an alternative transparent conducting electrode for optoelectronic device applications, *Vacuum*, 2022, **206**, 111487, DOI: **10.1016/j.vacuum.2022.111487**.

18 K. Li, Z. Huang and D. Zhu, Novel $Li_2Ga_{0.5}Sb_{0.5}O_3(Li_4GaS$-$bO_6)$:$Mn^{4+}$ phosphors with multisite occupancy for efficient FIR and luminescence lifetime dual-mode thermometers, *Ceram. Int.*, 2025, DOI: **10.1016/j.ceramint.2025.01.516**.

19 Z. Huang, K. Li, Z. Zhang, J. Liu and D. Zhu, Sr_4Ga-NbO_8:Mn^{4+}: a novel perovskite-structured red-emitting phosphor for a luminescence lifetime thermometer with good relative sensitivity and repeatability, *J. Mater. Chem. C*, 2025, **13**, 4564–4575, DOI: **10.1039/d4tc04916k**.

20 J. A. A. L. Jayarathna and K. R. Kaja, Energy-Harvesting Device Based on Lead-Free Perovskite, *AI, Comput. Sci. Rob. Technol.*, 2024, **3**, 1–9, DOI: **10.5772/acrt.20240036**.

21 A. Panda, K. K. Das, K. R. Kaja, M. Belal and B. K. Panigrahi, Single electrode mode triboelectric nanogenerator for recognition of animal sounds, *J. Met., Mater. Miner.*, 2024, **34**, 2170, DOI: **10.55713/JMMM.V34I4.2170**.

22 A. Panda, K. K. Das, K. R. Kaja, V. Gandi, S. Gourav Mohanty and B. K. Panigrahi, Low-cost high performance sustainable

triboelectric nanogenerator based on laboratory waste, *J. Met., Mater. Miner.*, 2025, **35**, e2226, DOI: **10.55713/jmmm.v35i1.e2226**.

23 K. R. Kaja, S. Hajra, S. Panda, M. A. Belal, P. Pakawanit, N. Vittayakorn, C. Bowen, H. Khanbareh and H. J. Kim, Triboelectrification Based on the Waste Waterproof Textiles for Multisource Energy Harvesting, *Adv. Sustainable Syst.*, 2024, 2400678, DOI: **10.1002/adsu.202400678**.

24 M. Rakshita, N. Madathil, A. A. Sharma, P. P. Pradhan, D. P. Kasireddi A. K., U. K. Khanapuram, R. K. Rajaboina and H. Divi, Phosphor-Based Triboelectric Nanogenerators for Mechanical Energy Harvesting and Self-Powered Systems, *ACS Appl. Electron. Mater.*, 2024, **6**, 1821–1828, DOI: **10.1021/acsaelm.3c01728**.

25 M. Rakshita, A. A. Sharma, P. P. Pradhan, K. A. K. Durga Prasad, K. Jayanthi and D. Haranath, Highly efficient and self-activating $Zn_3V_2O_8$ phosphor for the fabrication of cool-white light emitting devices, *Ceram. Int.*, 2023, **49**, 16775–16785, DOI: **10.1016/j.ceramint.2023.02.038**.

26 S. Rajkumar, E. Elanthamilan and J. P. Merlin, Facile synthesis of $Zn_3V_2O_8$ nanostructured material and its enhanced supercapacitive performance, *J. Alloys Compd.*, 2021, **861**, 157939, DOI: **10.1016/j.jallcom.2020.157939**.

27 C. Liu, Z. Zhou and Y. Zhang, Synthesis and luminescence properties of rare-earth free narrow band green emitting Na_2ZnSiO_4:Mn^{2+} phosphor for white LEDs, *J. Lumin.*, 2019, **213**, 1–5, DOI: **10.1016/j.jlumin.2019.04.060**.

28 L. K. Bharat, S. K. Jeon, K. G. Krishna and J. S. Yu, Rare-earth free self-luminescent $Ca_2KZn_2(VO_4)_3$ phosphors for intense white light-emitting diodes, *Sci. Rep.*, 2017, **7**, 1–9, DOI: **10.1038/srep42348**.

29 K. Singh, P. Pradhan, S. Priya, S. Mund and S. Vaidyanathan, Recent progress in trivalent europium (Eu^{3+})-based inorganic phosphors for solid-state lighting: an overview, *Dalton Trans.*, 2023, **52**, 13027–13057, DOI: **10.1039/d3dt00303e**.

30 W. M. Yen, S. Shionoya and H. Yamamoto, *Phosphor Handbook*, 2006.

31 R. J. Xie, N. Hirosaki, T. Suehiro, F. F. Xu and M. Mitomo, A simple, efficient synthetic route to $Sr_2Si_5N_8$:Eu^{2+}-based red phosphors for white light-emitting diodes, *Chem. Mater.*, 2006, **18**, 5578–5583, DOI: **10.1021/cm061010n**.

32 K. Ruthvik, A. Babu, P. Supraja, M. Navaneeth, V. Mahesh, K. Uday Kumar, R. Rakesh Kumar, B. Manmada Rao, D. Haranath and K. Prakash, High-performance triboelectric nanogenerator based on 2D graphitic carbon nitride for self-powered electronic devices, *Mater. Lett.*, 2023, **350**, 134947, DOI: **10.1016/j.matlet.2023.134947**.

33 K. R. Kaja, S. Hajra, S. Panda, M. A. Belal, U. Pharino, H. Khanbareh, N. Vittayakorn, V. Vivekananthan, C. Bowen and H. J. Kim, Exploring liquid–solid interface based triboelectrification, structures, and applications, *Nano Energy*, 2024, **131**, 110319, DOI: **10.1016/J.NANOEN.2024.110319**.

34 A. A. Tedstone, D. J. Lewis and P. O'Brien, Synthesis, Properties, and Applications of Transition Metal-Doped Layered Transition Metal Dichalcogenides, *Chem. Mater.*, 2016, **28**, 1965–1974, DOI: **10.1021/acs.chemmater.6b00430**.

35 P. Boutinaud, A. Barros and F. Kang, Luminescence depreciation in $ScVO_4$:Bi^{3+} upon irradiation in the Bi^{3+}-related absorption bands, *J. Lumin.*, 2022, **248**, 118941, DOI: **10.1016/j.jlumin.2022.118941**.

36 V. Chauhan, P. Deshmukh, S. Satapathy and P. C. Pandey, Greenish-yellow emission from rare-earth free Li^+ doped zinc vanadate phosphor, *Results Phys.*, 2022, **39**, 105689, DOI: **10.1016/j.rinp.2022.105689**.

37 L. Wu, P. Dai and D. Wen, New Structural Design Strategy: Optical Center VO_4-Activated Broadband Yellow Phosphate Phosphors for High-Color-Rendering WLEDs, *ACS Sustainable Chem. Eng.*, 2022, **10**, 3757–3765, DOI: **10.1021/acssuschemeng.2c00515**.

38 N. Baig, I. Kammakakam, W. Falath and I. Kammakakam, Nanomaterials: a review of synthesis methods, properties, recent progress, and challenges, *Mater. Adv.*, 2021, **2**, 1821–1871, DOI: **10.1039/d0ma00807a**.

39 M. Nadolska, M. Szkoda, K. Trzciński, P. Niedziałkowski, J. Ryl, A. Mielewczyk-Gryń, K. Górnicka and M. Prześniak-Welenc, Insight into Potassium Vanadates as Visible-Light-Driven Photocatalysts: Synthesis of V(IV)-Rich Nano/Microstructures for the Photodegradation of Methylene Blue, *Inorg. Chem.*, 2022, **61**, 9433–9444, DOI: **10.1021/acs.inorgchem.2c00136**.

40 P. Liu, J. Yi, R. Bao and D. Fang, A flower-like $Zn_3V_2O_8$/Ag composite with enhanced visible light driven photocatalytic activity: the triple-functional roles of Ag nanoparticles, *New J. Chem.*, 2019, **43**, 7482, DOI: **10.1039/c9nj00211a**.

41 V. Chauhan, P. Dixit and P. C. Pandey, Enhancement in greenish-white photoluminescence of $Zn_3(VO_4)_2$ phosphor by Bi^{3+} doping, *Optik*, 2021, **238**, 166682, DOI: **10.1016/j.ijleo.2021.166682**.

42 T. Nakajima, M. Isobe, T. Tsuchiya, Y. Ueda and T. Kumagai, A revisit of photoluminescence property for vanadate oxides AVO_3 (A:K, Rb and Cs) and $M_3V_2O_8$ (M: Mg and Zn), *J. Lumin.*, 2009, **129**, 1598–1601, DOI: **10.1016/j.jlumin.2009.03.029**.

43 S. Ni, X. Wang, G. Zhou, F. Yang, J. Wang and D. He, Crystallized $Zn_3(VO_4)_2$: synthesis, characterization and optical property, *J. Alloys Compd.*, 2010, **491**, 378–381, DOI: **10.1016/j.jallcom.2009.10.188**.

44 F. Du, W. Zhuang, R. Liu, J. Zhong, Y. Liu, Y. Hu, W. Gao, X. Zhang, L. Chen and K. Lin, Site occupancy and photoluminescence tuning of $La_3Si_{6-x}Al_xN_{11-x/3}$:$Ce^{3+}$ phosphors for high power white light-emitting diodes, *CrystEngComm*, 2017, **19**, 2836–2843, DOI: **10.1039/c7ce00435d**.

45 M. Rakshita, A. Babu, K. Jayanthi, S. Bathula, K. Uday Kumar and D. Haranath, Studies on contact angle measurements in superoleophobic aluminum hydroxide nanoflakes, *Mater. Lett.*, 2022, **315**, 131938, DOI: **10.1016/j.matlet.2022.131938**.

46 P. H. Kuo, N. A. Ley, M. L. Young and J. Du, Phase Evolution and Crystallization Mechanism of Glass Ceramic Solid-State Electrolyte from In Situ Synchrotron X-ray Diffraction, *J. Phys. Chem. C*, 2023, **127**, 17051–17062, DOI: **10.1021/acs.jpcc.3c02340**.

47 A. A. Sharma, M. Rakshita, P. P. Pradhan, K. A. K. D. Prasad, S. Mishra, K. Jayanthi and D. Haranath, Noninvasive treatment of psoriasis and skin rejuvenation using an akermanite-type narrowband emitting phosphor, *Luminescence*, 2023, **38**, 1–10, DOI: **10.1002/bio.4554**.

48 R. Devi Chandra, L. Veena and K. G. Gopchandran, Suppression of Visible Emission in Low-Temperature Synthesized Cobalt-Doped ZnO Nanoparticles and Their Photosensing Applications, *Inorg. Chem.*, 2023, **62**, 11360–11371, DOI: **10.1021/acs.inorgchem.3c00846**.

49 P. Luo, W. Zhang, S. Wang, G. Liu, Y. Xiao, C. Zuo, W. Tang, X. Fu and S. Dong, Electroactivation-induced hydrated zinc vanadate as cathode for high-performance aqueous zinc-ion batteries, *J. Alloys Compd.*, 2021, **884**, 161147, DOI: **10.1016/j.jallcom.2021.161147**.

50 D. A. Hoyos, A. Echavarría and C. Saldarriaga, Synthesis and structure of a porous zinc vanadate, $Zn_3(VO_4)_2 \cdot 3H_2O$, *J. Mater. Sci.*, 2001, **36**, 5515–5518, DOI: **10.1023/A:1012418706071**.

51 G. Maharana, R. Muniramaiah, J. Yuvashree, D. Mandal, S. Mondal, M. Kovendhan, J. M. Fernandes, G. Laxminarayana and D. P. Joseph, Tungsten and fluorine co-doping induced morphology change and textured growth of spray-pyrolyzed SnO_2 thin films viable for photocatalytic application, *Surf. Interfaces*, 2023, **42**, 103413, DOI: **10.1016/j.surfin.2023.103413**.

52 A. A. Sharma, M. Rakshita, P. P. Pradhan, K. A. K. Durga Prasad, S. Mishra, K. Jayanthi and D. Haranath, Efficacy of photodynamic therapy using UVB radiation-emitting novel phosphor material for non-surgical treatment of psoriasis, *J. Mater. Res.*, 2023, **38**, 2812–2822, DOI: **10.1557/s43578-023-01008-7**.

53 G. Chen, Y. Jin, L. Yuan, B. Wang, J. Huo, H. Suo, H. Wu, Y. Hu and F. Wang, Unlocking Cr^{3+}–Cr^{3+} Coupling in Spinel: Ultrabroadband Near-Infrared Emission beyond 900 nm with High Efficiency and Thermal Stability, *ACS Appl. Mater. Interfaces*, 2024, **16**, 30185–30195, DOI: **10.1021/acsami.4c03419**.

54 S. Wu, L. Yuan, G. Chen, C. Peng and Y. Jin, All-inorganic Mn^{2+}-doped metal halide perovskite crystals for the late-time detection of X-ray afterglow imaging, *Nanoscale*, 2023, **15**, 13628–13634, DOI: **10.1039/d3nr02208k**.

55 R. Babu, I. López-Fernández, S. Prasanthkumar and L. Polavarapu, All-Inorganic Lead-Free Doped-Metal Halides for Bright Solid-State Emission from Primary Colors to White Light, *ACS Appl. Mater. Interfaces*, 2023, **15**, 35206–35215, DOI: **10.1021/acsami.3c06546**.

56 M. M. Sajid, N. A. Shad, S. B. Khan, Z. Zhang and N. Amin, Facile synthesis of Zinc vanadate $Zn_3(VO_4)_2$ for highly efficient visible light assisted photocatalytic activity, *J. Alloys Compd.*, 2019, **775**, 281–289, DOI: **10.1016/j.jallcom.2018.10.134**.

57 S. S. Kalanur, I. H. Yoo, I. S. Cho and H. Seo, Effect of oxygen vacancies on the band edge properties of WO_3 producing enhanced photocurrents, *Electrochim. Acta*, 2019, **296**, 517–527, DOI: **10.1016/J.ELECTACTA.2018.11.061**.

58 A. Song, S. Liu, Q. Wang, D. Gao and J. Hu, Comprehensive evaluation of copper vanadate (α-CuV_2O_6) for use as a photoanode material for photoelectrochemical water splitting, *J Environ. Chem. Eng.*, 2023, **11**, 109892, DOI: **10.1016/j.jece.2023.109892**.

59 J. K. Cooper, S. Gul, F. M. Toma, L. Chen, Y. S. Liu, J. Guo, J. W. Ager, J. Yano and I. D. Sharp, Indirect bandgap and optical properties of monoclinic bismuth vanadate, *J. Phys. Chem. C*, 2015, **119**, 2969–2974, DOI: **10.1021/jp512169w**.

60 M. V. Malashchonak, E. A. Streltsov, D. A. Kuliomin, A. I. Kulak and A. V. Mazanik, Monoclinic bismuth vanadate band gap determination by photoelectrochemical spectroscopy, *Mater. Chem. Phys.*, 2017, **201**, 189–193, DOI: **10.1016/j.matchemphys.2017.08.053**.

61 S. Vijayakumar, S. H. Lee and K. S. Ryu, Synthesis of $Zn_3V_2O_8$ nanoplatelets for lithium-ion battery and supercapacitor applications, *RSC Adv.*, 2015, **5**, 91822–91828, DOI: **10.1039/c5ra13904j**.

62 T. Jeyakumaran, P. Sriramachandran, R. Shunmugavel and S. Ramaswamy, Synthesis and characterization of $Zn_3V_2O_8$ Yellow emitting nano phosphor by sol–gel method, *AIP Conf. Proc.*, 2017, **1832**, 10–13, DOI: **10.1063/1.4980338**.

63 P. Botella, F. Enrichi, A. Vomiero, J. E. Munõz-Santiuste, A. B. Garg, A. Arvind, F. J. Manjón, A. Segura and D. Errandonea, Investigation on the Luminescence Properties of $InMO_4$ ($M = V^{5+}$, Nb^{5+}, Ta^{5+}) Crystals Doped with Tb^{3+} or Yb^{3+} Rare Earth Ions, *ACS Omega*, 2020, **5**, 2148–2158, DOI: **10.1021/acsomega.9b02862**.

64 W. Li, Y. Zhuang, P. Zheng, T. L. Zhou, J. Xu, J. Ueda, S. Tanabe, L. Wang and R. J. Xie, Tailoring Trap Depth and Emission Wavelength in $Y_3Al_{5-x}Ga_xO_{12}$:Ce^{3+},V^{3+} Phosphor-in-Glass Films for Optical Information Storage, *ACS Appl. Mater. Interfaces*, 2018, **10**, 27150–27159, DOI: **10.1021/acsami.8b10713**.

65 D. Qu, D. Yang, Y. Sun, X. Wang and Z. Sun, White Emissive Carbon Dots Actuated by the H-/J-Aggregates and Förster Resonance Energy Transfer, *J. Phys. Chem. Lett.*, 2019, **10**, 3849–3857, DOI: **10.1021/acs.jpclett.9b01575**.

66 K. A. Denault, J. Brgoch, M. W. Gaultois, A. Mikhailovsky, R. Petry, H. Winkler, S. P. Denbaars and R. Seshadri, Consequences of optimal bond valence on structural rigidity and improved luminescence properties in $Sr_xBa_{2-x}SiO_4$:Eu^{2+} orthosilicate phosphors, *Chem. Mater.*, 2014, **26**, 2275–2282, DOI: **10.1021/cm500116u**.

67 A. Birkel, K. A. Denault, N. C. George, C. E. Doll, B. Héry, A. A. Mikhailovsky, C. S. Birkel, B. C. Hong and R. Seshadri, Rapid microwave preparation of highly efficient Ce^{3+}-substituted garnet phosphors for solid state white lighting, *Chem. Mater.*, 2012, **24**, 1198–1204, DOI: **10.1021/cm3000238**.

68 L. J. Yin, J. Dong, Y. Wang, B. Zhang, Z. Y. Zhou, X. Jian, M. Wu, X. Xu, J. R. Van Ommen and H. T. Hintzen, Enhanced Optical Performance of $BaMgAl_{10}O_{17}$:Eu^{2+} Phosphor by a Novel Method of Carbon Coating, *J. Phys. Chem. C*, 2016, **120**, 2355–2361, DOI: **10.1021/acs.jpcc.5b10215**.

69 H. S. Kim, K. Machida, M. Itoh and H. Hanzawa, Synthesis and Luminescence Properties of $(Sr,Ca)AlSiN_3$:Eu^{2+}

Phosphors under Atmospheric-Pressure, *ECS J. Solid State Sci. Technol.*, 2014, **3**, R234–R237, DOI: 10.1149/2.0061412jss.

70 K. A. K. D. Prasad, S. Puranjay, M. Rakshita, A. A. Sharma, P. P. Pradhan, K. U. Kumar, R. R. Kumar and D. Haranath, Simple and Cost-effective Synthesis of a Rare-earth Free Long Afterglow Phosphor for Dark Visual Markings, *J. Fluoresc.*, 2024, **35**, 867–875, DOI: 10.1007/s10895-023-03566-9.

71 N. Anitha, K. Jayanthi, M. Rakshita, A. A. Sharma, N. Jayarambabu, A. Akshaykranth, K. Babu, T. V. Rao, D. Dinakar and D. Haranath, Origin of the active luminescence from Sm^{3+}-activated borate phosphors: a correlational study of trap states and decay kinetics, *New J. Chem.*, 2022, **47**, 1472–1478, DOI: 10.1039/d2nj04601f.

72 P. Du, X. Wan, L. Luo, W. Li and L. Li, Thermally Stable Tb^{3+}/Eu^{3+}-Codoped $K_{0.3}Bi_{0.7}F_{2.4}$ Nanoparticles with Multi-color Luminescence for White-Light-Emitting Diodes, *ACS Appl. Nano Mater.*, 2021, **4**, 7062–7071, DOI: 10.1021/acsanm.1c01072.

73 W. Liu, H. Wu, H. Dong, Y. Jin, L. Yuan and Y. Jin, Achieving broadband near-infrared emission with superior anti-thermal quenching by optimizing the excited-state population of Cr^{3+} in $Gd_3ScGa_4O_{12}$ garnet phosphors, *Mater. Horiz.*, 2024, **11**, 6399–6407, DOI: 10.1039/d4mh01157k.

74 D. Qian, Y. Jin, Z. Li, H. Wu and Y. Hu, Constructing Broadband Near-Infrared Garnet Emitters $CaGd_2Ga_4SiO_{12}:Cr^{3+}$ with Unity Quantum Efficiency and High Thermal Stability for Versatile Applications, *Small*, 2025, **21**, e2411804, DOI: 10.1002/smll.202411804.

75 R. Guan, L. Cao, Y. You and Y. Cao, The Luminescence Properties and Energy Transfer from Ce^{3+} to Pr^{3+} for YAG:Ce^{3+},Pr^{3+} Phosphors, *J. Nanomater.*, 2015, 1–8, DOI: 10.1155/2015/549208.

76 C. C. Lin, Y. T. Tsai, H. E. Johnston, M. H. Fang, F. Yu, W. Zhou, P. Whitfield, Y. Li, J. Wang, R. S. Liu and J. P. Attfield, Enhanced Photoluminescence Emission and Thermal Stability from Introduced Cation Disorder in Phosphors, *J. Am. Chem. Soc.*, 2017, **139**, 11766–11770, DOI: 10.1021/jacs.7b04338.

77 K. Saidi, I. Kachou, K. Soler-Carracedo, M. Dammak and I. R. Martín, $Ba_2YV_3O_{11}$ Er^{3+}/Yb^{3+} Nanostructures for Temperature Sensing in the Presence of Bismuth Ions, *ACS Appl. Nano Mater.*, 2023, **6**, 17681–17690, DOI: 10.1021/acsanm.3c02911.

78 Y. Zhuang, C. Li, C. Liu, Y. Fu, Q. Shi, Y. Liang and L. Xia, High-efficiency YAG:Ce^{3+} glass-ceramic phosphor by an organic-free screen-printing technique for high-power WLEDs, *Opt. Mater.*, 2020, **107**, 110118, DOI: 10.1016/j.optmat.2020.110118.

79 C. De Mello Donegá, S. J. L. Ribeiro, R. R. Gonçalves and G. Blasse, Luminescence and non-radiative processes in lanthanide squarate hydrates, *J. Phys. Chem. Solids*, 1996, **57**, 1727–1734, DOI: 10.1016/0022-3697(96)00032-7.

80 R. N. Bhargava, D. Gallagher, X. Hong and A. Nurmikko, Optical properties of manganese-doped nanocrystals of ZnS, *Phys. Rev. Lett.*, 1994, **72**, 416–419, DOI: 10.1103/PhysRevLett.72.416.

81 D. Haranath, H. Chander, P. Sharma and S. Singh, Enhanced luminescence of $Y_3Al_5O_{12}:Ce^{3+}$ nanophosphor for white light-emitting diodes, *Appl. Phys. Lett.*, 2006, **89**, 1–4, DOI: 10.1063/1.2367657.

82 E. F. Schubert, Light Emitting Diodes and Solid-State Lighting, 2007, **12180**, 1–82.

83 J. Czajka and A. Szczeszak, Physicochemical Characterization of the Hybrid Molybdate-Tungstate Materials for Solid-State Lighting, *J. Phys. Chem. C*, 2023, **127**, 17415–17424, DOI: 10.1021/acs.jpcc.3c03482.

84 P. P. Pradhan, R. Muddamalla, A. A. Sharma, D. P. Durga, U. K. Khanapuram, R. K. Rajaboina and H. Divi, Rare-Earth Ion-Activated Nanostructured Fluorescent Marker for Easy Naked Eye Detection and Swift Imaging of Latent Fingerprints, *ACS Appl. Nano Mater.*, 2023, **6**, 19767–19776, DOI: 10.1021/acsanm.3c03578.

85 S. Berman, M. Navvab, M. Martin, J. Sheedy and W. Tithof, Comment on "A Comparison of traditional and high colour temperature lighting on the near acuity of elementary school children" by S Berman, M Navvab, MJ Martin, J Sheedy, and W Tithof, *Light: Res. Technol.*, 2006, **38**, 41–52, DOI: 10.1177/136578280603800114.